On the Energy Efficiency Potential of Multi-Actuated Electric Vehicles

Matteo Dalboni, Gil Martins, Davide Tavernini, Umberto Montanaro, Alessandro Soldati, Carlo Concari, Miguel Dhaens, and Aldo Sorniotti

***Abstract*—The literature shows increasing interest in the energy efficiency aspects of electric vehicles with multiple actuators, e.g., capable of individual wheel torque and rear-wheel-steering control, and proposes controllers considering the relevant vehicle power losses. However, the available studies lack systematic analyses on: i) the energy saving potential of the individual actuation methods, and their combinations; and ii) the operating conditions in which a set of actuators is particularly effective in reducing power consumption. This paper targets the identified gap. After providing background on the relevant power losses, three forms of actuation, i.e., torque-vectoring through two or four electric powertrains, active suspensions for front-to-total anti-roll moment distribution control, and rear-wheel-steering, are explored through a set of simulations in quasi-steady-state conditions, by using an experimentally validated high-fidelity non-linear vehicle model. The analysis covers a range of vehicle speeds, longitudinal and lateral accelerations, and tire-road friction conditions, and determines: a) the most energy-efficient understeer characteristics, i.e., the loci of the front steering angle as a function of lateral acceleration providing the minimum power consumption, for each set of actuators; b) the energy-efficient actuations for achieving given understeer characteristics; and c) the power consumption penalty of each considered configuration with respect to the one with the complete set of actuators.**

***Index Terms*—Electric vehicle, energy efficiency, torque-vectoring, active suspensions, rear-wheel-steering, two- and four-wheel-drive, understeer characteristic, control allocation.**

List of Symbols

a	Front semi-wheelbase.
b	Rear semi-wheelbase.
a_x	Longitudinal acceleration.
a_y	Lateral acceleration.
C	Cornering stiffness.
f	Front-to-total anti-roll moment distribution ratio.
F	Vertical force contributions at the wheel center generated by the suspension actuators.
f_{nom}	Nominal front-to-total anti-roll moment distribution ratio.
F_x	Longitudinal tire force.
F_y	Lateral tire force.
h_{CG}	Vehicle center of gravity height.
h_{roll}	Roll axis height at the longitudinal coordinate of the vehicle center of gravity.
J_x	Roll mass moment of inertia.
J_z	Yaw mass moment of inertia.
k	Fraction of the total roll moment that is compensated by the active suspension system.
k_d	Front-to-total wheel torque distribution ratio.
$k_{d,opt}$	Optimized front-to-total wheel torque distribution ratio.
m	Vehicle mass.
$M_{AR,Act}$	Anti-roll moment from the active suspension system on a specific axle.
$M_{AR,Act,Tot}$	Total anti-roll moment from the active suspension system.
M_z	Direct yaw moment.
P_{batt}	Battery power output toward the electric powertrains.
$P_{batt,inc}$	Battery power increase.
$\bar{P}_{batt,inc}$	Average battery power increase for a given lateral acceleration band.
$P_{batt,min}$	Battery power output on the minimum power envelope.
$P_{batt,opt}$	Battery power on the energy-efficient understeer characteristic.
$P_{EM,\max}$	Maximum electric motor power.
$P_{loss,EP}$	Electric powertrain power loss.
$P_{loss,EP,norm}$	Normalized electric powertrain power loss.
$P_{loss,x}$	Longitudinal tire slip power loss.
$P_{loss,x,norm}$	Normalized longitudinal tire slip power loss.
$P_{loss,y}$	Lateral tire slip power loss.
$P_{loss,y,norm}$	Normalized lateral tire slip power loss.
P_{mech}	Mechanical power output of the in-wheel powertrains.

Manuscript received 15 May 2023; revised 15 January 2024; accepted 11 March 2024. Date of publication 18 March 2024; date of current version 15 August 2024. This work was supported by the Horizon 2020 Programme of the European Commission under Grant 824250 (EVC1000 Project) and Grant 872907 (OWHEEL Project). The review of this article was coordinated by Prof. Josko Deur. *(Corresponding author: Aldo Sorniotti.)*

Matteo Dalboni is with the Department of Mechanical Engineering Sciences, University of Surrey, GU2 7XH Guildford, U.K., and also with the Department of Engineering and Architecture, University of Parma, 43121 Parma, Italy (e-mail: matteo.dalboni@studenti.unipr.it).

Gil Martins, Davide Tavernini, and Umberto Montanaro are with the Department of Mechanical Engineering Sciences, University of Surrey, GU2 7XH Guildford, U.K. (e-mail: gil.rpmartins@gmail.com; d.tavernini@surrey.ac.uk; u.montanaro@surrey.ac.uk).

Alessandro Soldati and Carlo Concari are with the Department of Engineering and Architecture, University of Parma, 43121 Parma, Italy (e-mail: alessandro.soldati@unipr.it; carlo.concari@unipr.it).

Miguel Dhaens is with the Advanced Chassis Research, Tenneco Automotive Europe, 3800 Sint Truiden, Belgium (e-mail: mdhaens@driv.com).

Aldo Sorniotti is with the Department of Mechanical and Aerospace Engineering, Politecnico di Torino, 10129 Torino, Italy (e-mail: aldo.sorniotti@polito.it).

Digital Object Identifier 10.1109/TVT.2024.3378154

r	Yaw rate.
R	Rolling radius of the tire.
R_l	Laden wheel radius.
T_{EM}	Electric motor torque.
$T_{EM,\max}$	Maximum electric motor torque.
$T_{EM,req}$	Electric motor torque request.
$T_{side,req}$	Total torque request on a vehicle side.
$T_{tot,req}$	Total torque demand.
t_w	Front and rear track widths.
V	Vehicle speed.
$v_{x,slip}$	Longitudinal slip speed.
$v_{y,slip}$	Lateral slip speed.
α	Tire slip angle.
β	Sideslip angle.
δ	Steering angle at the wheel.
δ_{sw}	Steering angle at the steering wheel.
$\mu_{\%}$	Tire-road friction factor, with 100% indicating dry tarmac conditions.
φ	Roll angle.
Ω	Motor speed.
$\Omega_{\max}$	Maximum motor speed.

Along the manuscript, the previous notations can be characterized by the subscripts $i = f, r$ and/or $j = l, r$, to specify whether the variable or parameter refers to a given axle ($i = f$, front axle; $i = r$, rear axle) or vehicle side ($j = l$, left-hand side; $j = r$, right-hand side).

I. Introduction

THE shift of the automotive industry towards electrification has resulted in a worldwide market penetration of electric vehicles (EVs) exceeding 13% in 2022 [1]. The cost of batteries and limited autonomy of EVs have motivated the development of advanced energy management systems, targeting power consumption reductions. Many control formulations from the recent literature focus on EVs with multiple actuators, mostly represented by two to four electric powertrains.

EVs with one motor per wheel enable the continuous controlled distribution of the torque levels between the two EV sides, commonly referred to as torque-vectoring (TV) or direct yaw moment control. The handling and active safety enhancements brought by TV are widely documented [2], [3], [4], [5]. Also, several studies, e.g., [6], discuss the influence of TV on the relevant power losses, namely the power losses in the electric powertrains, and those associated with longitudinal and lateral tire slip. Many energy-efficient control allocation (CA) algorithms have been proposed, which generate the total reference traction force and direct yaw moment, while minimizing the power losses in the electric powertrains [7], [8], [9], or indicators related to the longitudinal and lateral tire slip or tire workload distribution [10], [11], [12], [13], or combinations of the previous aspects [14], [15], [16], [17], [18]. While the conventional method is to reduce the power losses through CA, i.e., without modifying the cornering response, reference [15] shows that using TV to achieve energy-efficient understeer characteristics (UCs), i.e., the relationships between the front steering angle and lateral acceleration in quasi-steady-state conditions, brings additional power consumption savings, albeit at the consequence of influencing the cornering response.

Rear-wheel-steering (RWS) is another method to improve cornering agility and stability, either in isolation [19], [20], [21] or integrated with direct yaw moment control [22], [23], [24], [25]. Most of the RWS studies do not include any energy consideration. Exceptions are [25] and [26], which, however, focus on specific transient maneuvers, rather than the RWS power consumption reduction potential. In [27], dynamic programming minimizes the cornering resistance in step steer and sine-with-dwell tests, via front and rear steering as well as camber angle control. In [28] a genetic algorithm allocates the steering angles in a rescue vehicle, to obtain desirable cornering response and reduce tire slips. None of the previous studies discusses the first-principles of the impact of RWS on energy consumption.

Active suspension (AS) control, via individual actuators at the wheel corners or active anti-roll bars, has been demonstrated [29], [30], [31], [32], [33] for improving ride comfort and cornering response. The latter feature, achieved through the variation of the anti-roll moment distribution between the axles, has an impact on the lateral tire slip power losses, which, however, has not been investigated yet. The available studies [34], [35], [36] on the energy aspects of AS systems only consider the power consumption reductions achievable through efficient actuation, or energy recovery on irregular road profiles. An exception is [37], which focuses on AS kinematics, and explores the effect of camber angle on the power losses in cornering.

The handling authority of TV, RWS and AS, individually and in integrated form, has been covered in depth, e.g., in [38], [39], [40], which, however, do not analyze the energy consumption implications. An overview of the relevant literature is included in [41]. A few references, e.g., see [42], [43], [44], [45], [46], [47], propose integrated chassis controllers (ICCs) based on TV and different configurations for front and/or rear steering actuation or AS, with power consumption/loss or tire slip minimization. However, such references cover a limited set of actuators, e.g., see [48]. Moreover, the available results refer to specific maneuvers, and do not detail the power saving potential across the range of cornering and traction/braking conditions.

Hence, there is a gap in the literature in terms of: a) systematic evaluations of the energy saving capabilities of RWS and AS, in isolation and combined with TV for two- and four-wheel-drive (2WD and 4WD) EV configurations; and b) generation of energy-efficient UCs, for different combinations of chassis actuators. This study targets the identified gap, with the following contributions:

- The physical understanding of the influence of RWS on the lateral tire slip power losses through a novel single-track vehicle model, suitable for future controller design.
- The comparison of the potential effectiveness of different chassis actuations in terms of power consumption reduction, at multiple levels of longitudinal and lateral acceleration, vehicle speed, and tire-road friction. The identification of such potential cannot be achieved through the implementation of on-line energy-efficient ICCs, such

as the one in [48]. In fact, also in the most advanced nonlinear model predictive controllers, the approximations associated with the prediction models and the numerical solution of the control problem, imply significant margin of error, which makes difficult to derive general conclusions. The analysis of this paper significantly extends those in [10], [15], and [49], for TV systems in isolation.

- The analysis of the impact of the understeer characteristic on the power consumption, and the definition of energy-efficient UCs and CAs, associated with TV (including 2WD and 4WD cases), RWS and AS in isolation, and the combinations of the previous actuations. The objective is to find: a) the optimal cornering response and control effort distribution in terms of power consumption for each lateral acceleration, at assigned torque/speed/friction conditions; b) the variation of the power consumption as a function of the cornering response; and c) the additional benefit of using energy-efficient UCs, with respect to (w.r.t.) the conventional method of imposing energy-efficient CAs for given levels of understeer.

Notably, the output of this research is not represented by a set of control algorithms, which are the typical results of the available ICC analyses. In fact, as specified in the contributions, the ambition is to present a simulation-based routine – together with the respective set of outputs – to obtain the absolute minimum power consumption for selected set-ups of chassis actuators, understand how their action must be prioritized depending on the EV operating condition, and define the reference cornering response as a trade-off between desirable vehicle dynamics and energy consumption. Based on this solid foundation providing the achievable vehicle-level targets, the usual ICC development activity, which is not the object of this research, can be implemented a posteriori with increased awareness, and its results can be contrasted with the ideal behaviors generated through the novel methodology.

The specific investigation focuses on a case study EV with direct drive (without mechanical transmissions or clutches) in-wheel motors (IWMs), considered within the European project EVC1000. The manuscript is organized as follows: Section II provides the background on the relevant power loss contributions and chassis actuations; Section III describes the experimentally validated simulation environment and sets of quasi-steady-state simulations; Section IV discusses the postprocessing routines of the simulation data; Section V analyzes the results; finally, the main conclusions are drawn in Section VI.

II. Analytical Background and Preliminary Analyses With Simplified Models

A. Relevant Power Loss Contributions

The power losses that are affected by the actuators that will be analyzed in this study are:

- The electric powertrain power losses. At the EV level, the powertrain power loss, $P_{loss,EP}$, is expressed as the sum of the power losses of the individual powertrains, $P_{loss,EP,ij}$:

$$P_{loss,EP} = \sum_{i,j} P_{loss,EP,ij}\left(\Omega_{ij},\ T_{EM,ij}\right) \qquad (1)$$

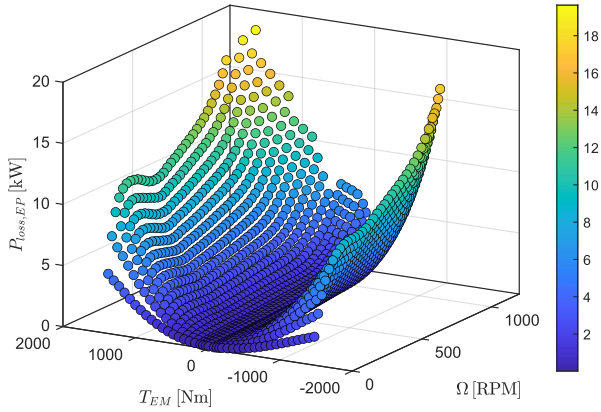

Fig. 1. Power loss map of an individual electric powertrain.

where the subscript $i = f,\ r$ designates the front or rear axle; the subscript $j = l, r$ indicates the left- or right-hand side of the EV; Ω_{ij} is the angular speed of the ij electric motor, which is coincident with the wheel speed for the direct drive IWMs of the case study EV; $T_{EM,ij}$ is the ij motor torque; and the notation '()' in (1) and the remainder indicates a function. $P_{loss,EP,ij}$ is in the form of maps, see the one in Fig. 1, provided by the suppliers of the in-wheel powertrains. The maps were experimentally measured and include the power loss contributions of the axial flux permanent magnet synchronous direct drive machine, respective inverter, and electrical wiring. They also consider the negative motor torque at zero current, resulting into a power loss caused by the iron losses and mechanical losses. As the electric powertrain power losses have been empirically obtained and embedded in a map, there is not any associated approximation related to the specific implementation. From $P_{loss,EP}$ and the mechanical IWM power, P_{mech}, it is possible to obtain the battery power output contribution, P_{batt}, for the operation of the electric powertrains:

$$P_{batt} = \sum_{i,j} \Omega_{ij}\, T_{EM,ij} + P_{loss,EP} = P_{mech} + P_{loss,EP} \qquad (2)$$

According to (2), the power consumption that is considered and minimized in the following analyses is the sum of those at the input of the traction inverters. This means that the power drawn by the systems other than the electric powertrains (e.g., cooling pumps, accessories, and chassis actuators, typically connected to a low-voltage system, which is linked to the traction battery through a dedicated DC/DC converter) as well as the battery power dissipations are neglected in the analysis. The approach does not imply any significant approximation in the computation of the optimal solution, since: i) the power requirement of the EV accessories and ancillaries is unaffected by the chassis actuation effort; ii) the variation of the power requirement related to the control effort of the considered chassis actuators is negligible, under the reasonable assumptions discussed later in this section; and iii) the losses within the traction battery and in the cablings from the energy storage

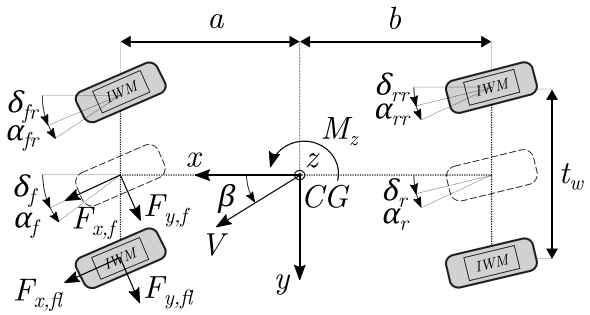

Fig. 2. Vehicle schematic with indication of the main variables. A single-track vehicle model schematic (indicated by dashed lines) is superposed to that of a double-track model of the EV with IWMs.

to the inverters are monotonically increasing functions of the inverter power input, and thus if the latter is reduced, the battery power loss will decrease proportionally.

- The longitudinal tire slip power loss, $P_{loss,x}$, i.e., the power loss at the EV level caused by the longitudinal tire slip:

$$P_{loss,x} = \sum_{i,j} -F_{x,ij}\ v_{x,slip,ij} \tag{3}$$

where $F_{x,ij}$ (see Fig. 2) and $v_{x,slip,ij}$ are the longitudinal force and longitudinal slip speed of the ij tire. $v_{x,slip,ij}$ is expressed as:

$$v_{x,slip,ij} = v_{x,ij} - \Omega_{ij}\ R \tag{4}$$

where $v_{x,ij}$ is the longitudinal component of the wheel hub speed in the tire reference frame; and R is the rolling radius of the tire.

- The lateral tire slip power loss, $P_{loss,y}$, i.e., the power loss related to the slip angle of each tire, which is given by:

$$P_{loss,y} = \sum_{i,j} -F_{y,ij} v_{y,slip,ij} \tag{5}$$

where $F_{y,ij}$ (see Fig. 2) and $v_{y,slip,ij}$ are the lateral force and lateral slip speed of the ij tire. $v_{y,slip,ij}$ is calculated as:

$$v_{y,slip,ij} = v_{x,ij}\ \tan\alpha_{ij} \tag{6}$$

where α_{ij} is the slip angle of the ij tire.

Equations (3)–(6) are based on the theory in [50], which derived the expression of the longitudinal and lateral tire slip power losses starting from the formulation of the well-known tire brush model, by integrating the product of the longitudinal and lateral forces per unit length by the respective relevant sliding speed between the tip of the brushes and the road surface, along the sliding region of the contact patch. The results of such integration are represented by (3) and (5), which have also been used in many other chassis control studies from the literature, e.g., see [2], [10], [51]. Although considered in the simulations of this study, the total power loss associated with tire rolling resistance, being a function of EV speed and vehicle weight, is not affected by the actuators, unless tires with different rolling resistance properties are installed on the two axles, which is not the case for the specific EV.

B. Effect of Torque-Vectoring

The purpose of TV is to generate a desired direct yaw moment, M_z, by manipulating the wheel torque requests, $T_{EM,req,ij}$, for each IWM, while achieving the total wheel torque demand, $T_{tot,req}$, at the EV level, from the human driver or automated driving system. In the remainder, the individual IWM torque demands are computed through:

$$T_{EM,req,fl} = k_{d,l}\ \left[\frac{T_{tot,req}}{2} - \frac{R_l}{t_w}M_z\right] \tag{7}$$

$$T_{EM,req,fr} = k_{d,r}\ \left[\frac{T_{tot,req}}{2} + \frac{R_l}{t_w}M_z\right] \tag{8}$$

$$T_{EM,req,rl} = [1-k_{d,l}]\ \left[\frac{T_{tot,req}}{2} - \frac{R_l}{t_w}M_z\right] \tag{9}$$

$$T_{EM,req,rr} = [1-k_{d,r}]\ \left[\frac{T_{tot,req}}{2} + \frac{R_l}{t_w}M_z\right] \tag{10}$$

where t_w is the track width, assumed the same on the front and rear axles; R_l is the laden tire radius; and $k_{d,j}$ is the front-to-total wheel torque distribution coefficient within each EV side.

Through the powertrain torque distribution, TV has an impact on $P_{loss,EP}$. For given vehicle speed and $T_{tot,req}$, the value of M_z that minimizes the powertrain losses is a function of the powertrain characteristics. As the power loss maps depend on the powertrain set-up, and can have rather complex shapes, including convex and non-convex regions, the energy-efficient TV solution from the viewpoint of the electric powertrains cannot be derived through analytical methods, unless assumptions are made on the power loss maps [15].

TV also has an impact on: a) $P_{loss,x}$, as the individual wheel torque specified by the TV system, together with the vertical tire load and slip angle, induces a corresponding value of $v_{x,slip,ij}$; and b) $P_{loss,y}$, as M_z has an influence on the front and rear slip angles, α_f and α_r, which can be expressed through the following simplified equations, resulting from a linear single-track vehicle model formulation in steady-state cornering [52]:

$$\alpha_f = -\frac{ma_y b}{C_f\,[a+b]} + \frac{M_z}{C_f\,[a+b]} \tag{11}$$

$$\alpha_r = -\frac{ma_y a}{C_r\,[a+b]} - \frac{M_z}{C_r\,[a+b]} \tag{12}$$

where C_f and C_r are the front and rear cornering stiffness; a and b are the front and rear semi-wheelbases; m is the vehicle mass; and a_y is the lateral acceleration. Under the assumption of linear tire behavior, Kobayashi et al. [13] demonstrate that 'the minimization control of the tire slip power loss requires the equalization of the tire slip velocity vectors', i.e., the longitudinal and lateral slip speeds must be the same on the four tires. However, they do not directly provide analytical formulations of the optimal M_z for a generic EV in pure cornering. This can be obtained from the simplified expression of $P_{loss,y}$ for a linear single-track model:

$$P_{loss,y} = C_f\ \alpha_f^2 V + C_r \alpha_r^2 V \tag{13}$$

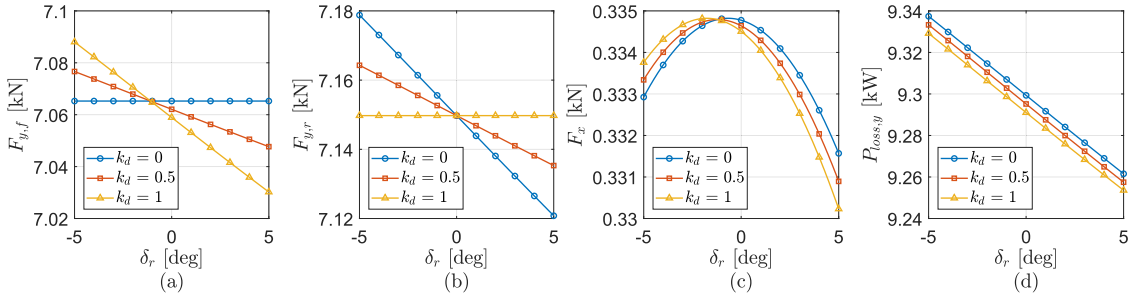

Fig. 3. Effect of the rear wheel steering angle, δ_r, for different values of the longitudinal force distribution coefficient, k_d, in steady-state cornering conditions, with $a_y = 5$ m/s^2, $V = 100$ km/h, and $M_z = 0$ Nm. (a) Lateral force of the front axle, $F_{y,f}$; (b) lateral force of the rear axle, $F_{y,r}$; (c) total longitudinal force, F_x; and (d) total lateral tire slip power loss, $P_{loss,y}$. $C_f = 300$ kN/rad, $C_r = 304$ kN/rad.

where V is vehicle speed. By substituting (11) and (12) into (13) and imposing $dP_{loss,y}/dM_z = 0$, the direct yaw moment minimizing the lateral tire slip power loss, $M_{z,loss,y,\min}$, is:

$$M_{z,loss,y,\min} = \frac{ma_y\left[\frac{b}{C_f} - \frac{a}{C_r}\right]}{\frac{1}{C_f} + \frac{1}{C_r}} \tag{14}$$

which neglects the longitudinal tire slip power loss, and is meaningful only in the linear range of the cornering response, whereas TV systems are very effective and often used at medium-to-high a_y.

C. Effect of Rear-Wheel-Steering

According to the conventional linear single-track vehicle model [52], for a given a_y value, $P_{loss,y}$ is independent of the front and rear steering angles, δ_f and δ_r. Therefore, to consider the effect of δ_r on the power losses, a novel nonlinear simplified bicycle model formulation is proposed for steady-state cornering, which includes the longitudinal force, lateral force, and yaw moment balance equations:

$$-mrV\beta = F_x + C_f\alpha_f\delta_f + C_r\alpha_r\delta_r \tag{15}$$

$$mrV = -C_f\alpha_f - C_r\alpha_r + k_dF_x\delta_f + [1-k_d]\,F_x\delta_r \tag{16}$$

$$0 = [-C_f\alpha_f + k_dF_x\delta_f]\,a - \{-C_r\alpha_r + [1-k_d]\,F_x\delta_r\}\,b + M_z \tag{17}$$

where β is the sideslip angle; r is the yaw rate; and k_d is the front-to-total longitudinal force distribution coefficient (or wheel torque distribution coefficient, if the laden tire radius is assumed to be the same on the two axles) of the single-track vehicle model, such that the front and rear longitudinal tire forces, $F_{x,f}$, and $F_{x,r}$, are expressed as functions of the total longitudinal force, F_x, through $F_{x,f} = k_d\,F_x$ and $F_{x,r} = [1-k_d]\,F_x$. The aerodynamic drag and rolling resistance force are not included in (15); nevertheless, they would not change the outcome of the analysis.

The model follows the small-angle approximation; hence, $k_dF_x\delta_f$ and $[1-k_d]F_x\delta_r$ in (16) and (17) are the components of the EV traction or braking forces along the y-axis of the vehicle reference system. Similarly, $C_f\alpha_f\delta_f$ and $C_r\alpha_r\delta_r$ are the components of the lateral axle forces along the x-axis of the reference frame. For simplicity, the front and rear lateral axle forces, $F_{y,f}$ and $F_{y,r}$, are considered to be linear functions of α_f and α_r, i.e., $F_{y,f} = -C_f\alpha_f$ and $F_{y,r} = -C_r\alpha_r$, and the following expressions are used for the front and rear slip angles:

$$\alpha_f = -\delta_f + \beta + \frac{ra}{V} \tag{18}$$

$$\alpha_r = -\delta_r + \beta - \frac{rb}{V} \tag{19}$$

Despite its simplicity, the model does not bring a concise analytical solution. A numerical approach to (15)–(19) provides the results in Fig. 3, for $a_y = 5$ m/s^2, $V = 100$ km/h, and $M_z = 0$ Nm. The figure displays $F_{y,f}$, $F_{y,r}$, F_x, and $P_{loss,y}$, as functions of δ_r, for three values of k_d. The results show that: a) only the lateral force of the driven axle/s varies with δ_r; b) regardless of the longitudinal force distribution, the more the rear wheel is steered in-phase, i.e., in the same direction as δ_f, the more $P_{loss,y}$ decreases; and c) the front-wheel-drive configuration implies less lateral tire slip power loss than the rear-wheel-drive one, which is consistent with the simulations in [25].

A physical interpretation can be inferred from (16) and (17). If M_z is neglected, by imposing $a_y = rV$ (steady-state cornering) and rearranging, α_f and α_r are given by:

$$\alpha_f = \frac{1}{C_f}\left[-ma_y\frac{b}{a+b} + k_dF_x\delta_f\right] \tag{20}$$

$$\alpha_r = \frac{1}{C_r}\left\{-ma_y\frac{a}{a+b} + [1-k_d]\,F_x\delta_r\right\} \tag{21}$$

For a rear-wheel-drive vehicle, $k_d = 0$ holds, and thus, based on (20), α_f only depends on a_y, i.e., RWS actuation does not change the front lateral tire slip power loss. Conversely, α_r is a linear function of δ_r, as the component of $F_{x,r}$ along the y-axis of the vehicle reference system modifies the magnitude of the rear lateral force, $F_{y,r}$, required to meet the lateral force and yaw moment balance equations. From (21), $a_y > 0$ implies a negative α_r contribution, while in-phase rear steering, i.e., $\delta_r > 0$, implies a positive α_r contribution (this is true for any $0 \le k_d \le 1$ and $F_x \ge 0$), which reduces the magnitude of the rear lateral slip, and thus the respective power loss contribution, according to (5) and (13).

In a front-wheel-drive vehicle, i.e., for $k_d = 1$, the rear steering angle has no effect on α_r, whereas α_f is a linear function of δ_f. In fact, by assuming $|-ma_y b/(a+b)| > |F_x \delta_f|$, which is typical of normal operation, based on (20) $F_{y,f}$ and $|\alpha_f|$ decrease if δ_f is increased, because of the lateral component of the longitudinal tire force in the vehicle reference system. However, since the comparison in Fig. 3 is carried out for a given lateral acceleration level, the beneficial increment of δ_f must be accompanied by a corresponding increase of δ_r, to keep $a_y = 5$ m/s^2. The relationship between δ_f and δ_r to maintain a_y constant and equal to its assigned value is derived by considering the difference between (18) and (19):

$$\alpha_f - \alpha_r = -\delta_f + \delta_r + \frac{a_y\,[a+b]}{V^2} \tag{22}$$

By plugging (20) and (21) into (22), the following condition is obtained:

$$\delta_f - \frac{C_f}{F_x + C_f}\,\delta_r = \frac{C_f}{F_x + C_f}\left\{\frac{ma_y}{C_f}\frac{b}{a+b} - \frac{ma_y}{C_r}\frac{a}{a+b} + \frac{a_y\,[a+b]}{V^2}\right\} \tag{23}$$

which shows that the locus of the operating points corresponding to a fixed a_y implies a constant value of $\delta_f - \delta_r C_f/[F_x + C_f]$. Hence, for an assigned a_y, if δ_r is increased, δ_f must be correspondingly increased, which brings the reduction of $F_{y,f}$ in Fig. 3(a), and $P_{loss,y}$ in Fig. 3(d).

The conditions $0 < k_d < 1$, corresponding to a 4WD vehicle, imply the superposition of the effects discussed for the special cases with $k_d = 0$ and $k_d = 1$.

Given the small magnitude of the actuator displacements, at the vehicle level RWS actuation implies negligible power loss w.r.t. the tire slip power loss contributions. From an application viewpoint, (15)–(23) could be used as prediction model for the model predictive control of four-wheel-steering vehicles, which would enable consideration of the trade-off between energy efficiency and vehicle dynamics.

D. Effect of Active Suspension Control

According to the industrial practice in suspension control, the total anti-roll moment that is provided by the AS system is computed as:

$$M_{AR,Act,Tot} = k m a_y\,[h_{CG} - h_{roll}] \tag{24}$$

where the nondimensional coefficient k ($k = 0.9$ in this study) expresses the fraction of the total roll moment that is compensated by the suspension actuators, i.e., $k = 0$ indicates absence of roll moment compensation, $k = 1$ indicates complete compensation, which corresponds to theoretically zero roll angle, and $k > 1$ corresponds to overcompensation, with the vehicle body leaning towards the inner side of the turn; h_{CG} is the center of gravity height; and h_{roll} is the roll axis height at the longitudinal coordinate of the vehicle center of gravity.

The front and rear active anti-roll moments are computed as:

$$M_{AR,Act,f} = f M_{AR,Act,Tot} \tag{25}$$

$$M_{AR,Act,r} = [1-f]\; M_{AR,Act,Tot} \tag{26}$$

where f is the front-to-total anti-roll moment distribution coefficient. The corresponding equivalent vertical force contributions at the wheel center are given by:

$$F_{ij} = \mp \frac{M_{AR,Act,i}}{t_w} \tag{27}$$

The variation of f, achievable through AS systems, has a nonlinear effect on the cornering response, i.e., the level of understeer in steady-state and transient conditions, and thus on the tire slip power losses. Only the recent literature [31] has proposed accurate models for the design of front-to-total anti-roll moment distribution controllers. The involved relationships cannot be described by explicit formulations. In fact, the analysis of the AS effect requires a planar model with four wheels and a non-linear tire model.

In the considered EV demonstrator, the active anti-roll moments are generated by the next generation set-up of the Kinetic system by Tenneco Automotive, which also includes passive valves that are responsible for suspension damping. Passive springs are installed in parallel to the AS actuators to provide the conventional level of stiffness. The generation of the active anti-roll moment corresponds to non-negligible power consumption. In this study, all considered EV configurations are characterized by AS actuation, with the purpose of reducing the roll angle caused by a_y, according to (24). In the baseline configurations, f is kept constant and equal to a nominal value, $f_{nom} = 0.68$, providing a cornering response similar to the EV without AS actuators. As the actuation power is mainly related to the total active anti-roll moment rather than its distribution among the axles, in the following analyses the consumption of the AS system is neglected, since it is approximately the same for all EV configurations.

E. Motivations for an Extensive Simulation Study With an Advanced Vehicle Model

The previous subsections analyzed the power loss effects of TV, RWS and AS from a simplified perspective. However, the models described so far are based on significant assumptions. Especially in the nonlinear region of vehicle operation and for multiple actuators, the underlying physics do not allow clear and immediate understanding. Hence, the quantitative evaluation of the effects of different combinations of actuators justifies the need for a non-linear model. Therefore, this study is based on an extensive and systematic set of simulations carried out through the high-fidelity model in Section III.

III. Advanced Simulation Set-Up

A. High-Fidelity Vehicle Model

The high-fidelity EV model was implemented through the vehicle simulation package VSM by AVL. The model accounts for the degrees of freedom of the sprung and unsprung masses as well as suspension elasto-kinematics and electric powertrain efficiency characteristics. The tires are modeled through version 5.2 of the Pacejka magic formula, considering the tire force

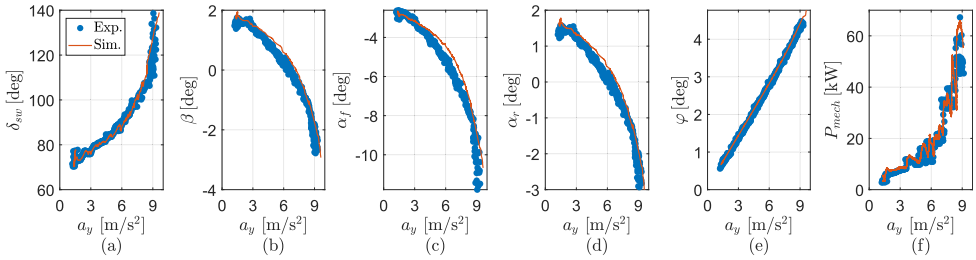

Fig. 4. Experimental validation of the high-fidelity simulation model along a 40 m skidpad test. (a) Understeer characteristic, i.e., steering wheel angle δ_{sw} as a function of lateral acceleration, a_y; (b) sideslip characteristic, i.e., sideslip angle β as a function of a_y; (c) front sideslip characteristic, i.e., front slip angle α_f as a function of a_y; (d) rear sideslip characteristic, i.e., rear slip angle α_r as a function of a_y; (e) roll characteristic, i.e., roll angle φ as a function of a_y; and (f) mechanical power characteristic, i.e., mechanical power P_{mech} as a function of a_y. The dots represent the experimental data ('Exp.'); the continuous lines are the simulation results ('Sim.').

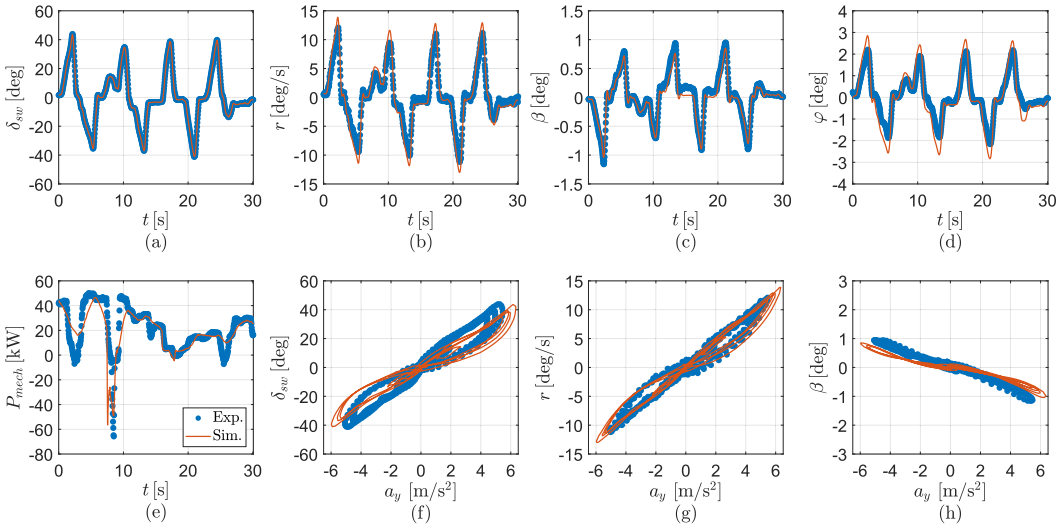

Fig. 5. Experimental validation of the high-fidelity simulation model along a transient maneuver at a vehicle speed V of approx. 100 km/h. (a) Steering wheel angle δ_{sw}; (b) yaw rate r; (c) sideslip angle β; (d) roll angle φ; and (e) mechanical power P_{mech}, expressed as functions of time t. (f) δ_{sw}; (g) r; and (h) β, as functions of a_y.

TABLE I
MAIN EV PARAMETERS

Description	Symbol	Value
Vehicle mass	m	2843 kg
Vehicle center of gravity height	h_{CG}	0.63 m
Front and rear track widths	t_w	1.66 m
Front semi-wheelbase	a	1.47 m
Rear semi-wheelbase	b	1.46 m
Wheel radius	R	0.37 m
Roll mass moment of inertia	J_x	550 kg m^2
Yaw mass moment of inertia	J_z	5291 kg m^2
Maximum motor speed	Ω_{max}	1300 RPM
Maximum motor torque	$T_{EM,max}$	1500 Nm
Maximum motor power	$P_{EM,max}$	146 kW

nonlinearities in purely longitudinal and lateral operating conditions, including the saturation of the longitudinal and lateral tire forces, as well as the tangential force coupling effects, corresponding to the tire friction ellipse. W.r.t. the transient response, the model embeds tire relaxation phenomena, with different and appropriate dynamics for the longitudinal and lateral tire forces. The vehicle tire parametrization values were directly provided by the car maker involved in the EVC1000 project.

The main EV parameters are reported in Table I. The modeled EV configuration with IWMs is the conversion of a pre-existing production EV with two on-board powertrains. The model of the original EV was experimentally validated, e.g., in the skidpad in Fig. 4 and transient steering test in Fig. 5. The vehicle is understeering despite having a mass distribution marginally biased toward the rear axle, since the equivalent roll stiffness is significantly biased toward the front axle. In fact, the front-to-total anti-roll moment distribution ratio of the passive and active suspension components of the baseline vehicle is 0.68, which is significantly larger than the front-to-total mass distribution, amounting to ∼0.5. For a given lateral acceleration, this set-up increases the lateral load transfer on the front axle, which reduces its lateral force capability, and thus increases the slip angle magnitude. In the skidpad test, across the lateral acceleration range, the average root mean square error value between model and experiments amounts to 3.9 deg in terms of steering wheel angle, 0.29 deg in terms of sideslip angle, and 0.08 deg in terms of roll angle. In the sinusoidal steering test, the root mean square values of the yaw rate, sideslip angle e roll angle errors – computed over time – amount to 1.33 deg/s, 0.09 deg, and 0.45 deg. The good match between simulations and experiments

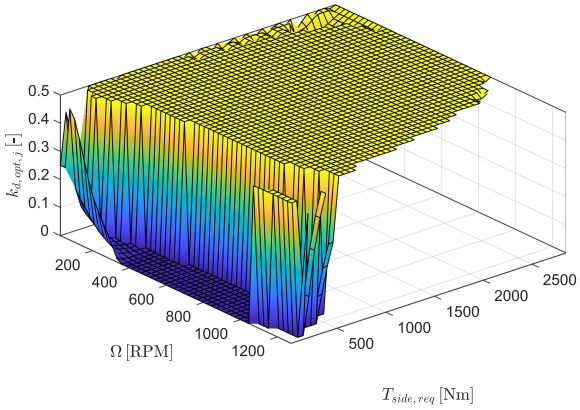

Fig. 6. Optimal side torque request distribution in motoring conditions.

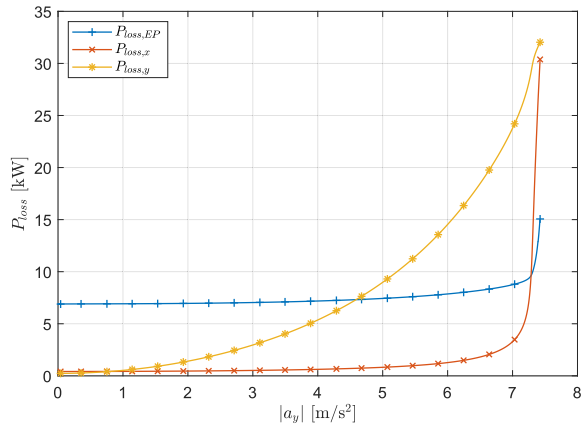

Fig. 7. Power losses during a ramp steer maneuver at $a_x = 1.5$ m/s^2 and $V = 100$ km/h, for the baseline 4WD EV ($M_z = 0$, $\delta_r = 0$, and $f = 0.68$), in high tire-road friction conditions.

covers the cornering response, and aspects related to the power losses and energy consumption, e.g., see the profiles of the front and rear slip angles, α_f and α_r, and the total mechanical powertrain power, P_{mech}, reported in the figures. The validation also included the execution of driving cycles on a rolling road facility.

For the IWM EV, both the 2WD and 4WD operations are considered, to assess the efficiency effect of the front-to-total wheel torque distribution. The 2WD case, corresponding to the rear-wheel-drive operation of the EV, is modeled by deactivating the front powertrains, i.e., the EV inertial properties are the same as for the 4WD IWM case. For a given direct yaw moment, the 4WD configuration is free to allocate the torque among the two wheels on the same side, e.g., according to energy efficiency or vehicle dynamics criteria.

The IWM torque distribution within each side of the 4WD case is achieved through an offline-generated map of the front-to-total wheel torque distribution coefficient, minimizing the power loss of the two powertrains of the same EV side, as a function of the motor speed, Ω, which is approximately the same for the two machines, and side torque demand, $T_{side,req}$, according to:

$$k_{d,opt,j} = \underset{k_{d,j}}{\operatorname{argmin}} \left(P_{loss,EP,fj}\left(\Omega, k_{d,j} T_{side,req}\right) + P_{loss,EP,rj}\left(\Omega, \left[1 - k_{d,j}\right] T_{side,req}\right)\right) \quad (28)$$

where $k_{d,j}$ is the front-to-total torque distribution ratio value for the j EV side, within the high-fidelity VSM double-track model (i.e., $k_{d,j}$ – already adopted in the TV formulations in (7)–(10) in Section II-B – is the equivalent of the coefficient k_d used in the single-track model analysis in Section II-C), and $k_{d,opt,j}$ is its optimal value. For the considered powertrain, the process provides the map in Fig. 6, for the case of traction. A similar map is derived for regeneration. For most of the speed range (up to ~1000 RPM), $k_{d,opt,j}$ is zero at low side torque requests, i.e., only the rear powertrain is used; while $k_{d,opt,j}$ is 0.5 elsewhere.

The result is consistent with the available TV literature, e.g., see [15], [51], [53], which show – under specific assumptions – that the optimal solution is a progressive switching of an increasing number of IWMs. Since the wheel torque distributions are similar to those obtained in the previous references dealing with on-board powertrains with different electric machine technologies, the generality of the analysis for a wide range of powertrains can be inferred. As (28) was solved through brute force optimization for a dense grid of $k_{d,j}$ values, and the power loss maps were experimentally measured, the optimal torque distribution is not affected by assumptions related to the powertrains. The main simplification is to neglect longitudinal tire slip, which holds up to the high lateral acceleration range. From the powertrain efficiency viewpoint, the conditions $k_{d,opt,j} = 0$ and $k_{d,opt,j} = 1$ are equivalent, but, given the high torque rating of the specific IWMs, the rear-wheel-drive operation is prioritized to maximize traction, given the ~50% static front-to-total weight distribution. In fact, the longitudinal load transfer associated with the traction torque increases the tire load on the rear axle. Hence, the rear-wheel-drive operation of the vehicle for low torque demands is associated with a longitudinal tire slip reduction with respect to the front-wheel-drive operation.

B. Maneuver Set-Up

The high-fidelity model was set up to evaluate the power consumption in quasi-steady-state cornering, simulated through ramp steer tests, in which, after an initial longitudinal acceleration in straight line to bring the EV to the target speed, V is kept constant, while δ_{sw} is varied according to a slow ramp at a rate of 5 deg/s. To consider the effect of the longitudinal vehicle acceleration a_x on the power losses, an external force, $F_{ext} = -ma_x$, equivalent to the inertial force, is applied to the EV center of gravity, while imposing constant speed through the VSM driver model. Such an approach to non-zero a_x conditions considers the correct steady-state vertical tire load and slip ratio distributions, without the interferences caused by variable EV speed operation. In the literature, similar methods have been used through the implementation of quasi-static models [2], [10] and the application of the Milliken moment method [52].

The simulation approach enables to map the power losses and P_{batt} as functions of V, a_x, and a_y. For example, Fig. 7 shows the dependency of $P_{loss,EP}$, $P_{loss,x}$, and $P_{loss,y}$ on a_y, for $a_x = 1.5$ m/s^2 and $V = 100$ km/h. $P_{loss,EP}$ and $P_{loss,x}$ are monotonically increasing with a gentle slope up to $a_y \sim 7$ m/s^2, with the latter having lower magnitude. The two curves experience a significant gradient increase above 7 m/s^2, when

TABLE II
ACTUATION LEVELS IN THE RAMP STEER SIMULATION CAMPAIGN

	Min. value	Max. value	Unit	No. of pts
M_z	-2	2	kNm	9
δ_r	-2	2	deg	11
f	0.2	0.8	-	6

the cornering limit is approached, as the internal driven wheels spin because of their reduced vertical load. On the contrary, $P_{loss,y}$ increases throughout the $|a_y|$ domain, according to the increments of lateral tire forces and slip angles.

C. Simulation Campaign

Since the considered EV is a large sport utility vehicle, the simulation campaign focuses on conditions of relatively high vehicle speed, zero or low longitudinal acceleration, and rather high tire-road friction, typical of highway operation. The selected ramp steer maneuvers cover a representative combination of vehicle speeds (V = 50, 100, and 120 km/h), longitudinal accelerations (a_x = 0 and 1.5 m/s^2), tire-road friction conditions (the tire-road friction factor, $\mu_{\%}$, was set to 100% and 70%), and independent or combined interventions of TV, RWS, and AS, for a total of seven actuation combinations, indicated in the remainder as M_z, δ_r, f, $M_z+\delta_r$, M_z+f, δ_r+f, and $M_z+\delta_r+f$, which reflect the respective control actions. The actuation levels, which are constant within each ramp steer, are specified in Table II, and are realistic for the specific EV. In the tests involving RWS, the same steering angle is applied to both rear wheels. This violation of the Ackermann steering geometry is justified by the small angles. For each maneuver and chassis actuation combination, both the 2WD and 4WD EV cases were simulated. In summary, the campaign considered 594 actuation levels (corresponding to the combination of 9 values of M_z, 11 values of δ_r, and 6 values of f, see Table II), 2 powertrain configurations (2WD and 4WD), and 12 operating conditions (corresponding to 3 values of V, 2 values of a_x, and 2 values of $\mu_{\%}$), for a total number of 14256 simulations. The baseline 2WD and 4WD EV configurations correspond to $M_z = 0$ ($k_{d,opt,j}$ is adopted for the front-to-total wheel torque distribution in the 4WD case), $\delta_r = 0$, and $f = f_{nom} = 0.68$, and are used as benchmarking settings in the remainder.

IV. POST-PROCESSING METHODOLOGY

In addition to the accuracy of the model, the trustworthiness of the analysis depends on the objectivity and robustness of the automated post-processing method of the results. The post-processing routine consists of the following steps:

- Identification of the significant part of each ramp steer, i.e., only the data following the beginning of the steering wheel angle application are considered. Moreover, the final portion of the datapoints of each test is excluded. This condition is triggered when the EV exceeds 90% of the maximum lateral acceleration achieved during the maneuver. In fact, in the operating region at and beyond the limit of handling, the data could be unreliable due to the high longitudinal tire slips, and the related dynamics.

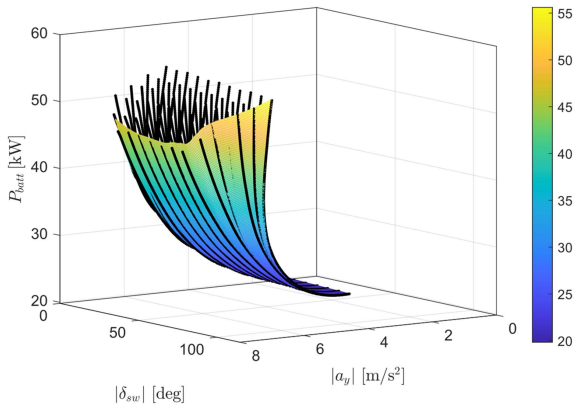

Fig. 8. Example of minimum power envelope (the color scale indicates P_{batt} in kW), i.e., the bottom envelope of the curves corresponding to the UCs with minimum power consumption for the 2WD EV with $\delta_r + f$, for V = 100 km/h, zero a_x, and $\mu_{\%} = 70\%$.

- Determination of the energy-efficient UCs, $\delta_{sw,opt}(a_y)$, i.e., the loci of δ_{sw} for which the battery power consumption is minimum at each considered a_y, for given a_x, V, and $\mu_{\%}$ values, and chassis actuator suite. For an operating condition, the energy-efficient UC is extracted from the relevant bundle of N discrete UCs, each of them corresponding to an individual ramp steer simulation. Therefore, $\delta_{sw,opt}(a_y)$ is the result of the concatenation of portions of different UCs, i.e., the most efficient one for each a_y. In the extraction phase, the points of the N UCs are interpolated to have them defined for the same lateral acceleration vector, $\mathbf{a_y} = [a_{y,1}\ a_{y,2}..a_{y,k}\ldots a_{y,k_{P,\max}}]$. Following interpolation, the generic point $\delta_{sw,opt}(a_{y,k})$ of the energy-efficient UC is computed as:

$$\begin{aligned}&\delta_{sw,opt}\ (a_{y,k})\\&=\underset{\delta_{sw}}{\operatorname{argmin}}\left(P_{batt}\left(\delta_{sw,1}\left(a_{y,k}\right)\right), P_{batt}\left(\delta_{sw,2}\left(a_{y,k}\right)\right), \ldots,\right.\\&\left.P_{batt}\left(\delta_{sw,n}\left(a_{y,k}\right)\right), \ldots, P_{batt}\left(\delta_{sw,N}\left(a_{y,k}\right)\right)\right)\end{aligned} \tag{29}$$

A moving average filter is applied to the resulting sequence of optimal points, to smoothen the characteristics.

- Computation of the minimum power envelope. For a multi-actuated EV, it is possible to achieve the same working point (a_y, δ_{sw}), i.e., the same UC, through different blends of the available actuations, the so-called control allocations.

The corresponding P_{batt} value differentiates the multiple CAs providing the same cornering response. The minimum power envelope is the surface of the points with the lowest P_{batt} value for each achievable working point (a_y, δ_{sw}), for a given actuator set-up and a_x, V, and $\mu_{\%}$. An example of surface is provided in Fig. 8. Because of its continuous nature, the minimum power envelope fills the gaps between the curves corresponding to individual ramp steer simulations, see the lines in the figure, thus providing the best approximation of the minimum power usage for the infinite number of UCs laying on its surface. The routine, whose pseudo-code is provided in Algorithm 1, consists of the following steps:

Algorithm 1: Extraction of the Minimum Power Envelope.

Repartition of the (a_y, δ_{sw}) domain into bins and identification of the minimum power consumption point in each bin

for i_{mr} from 1 to N_{mr}
  for j_b from 1 to no. of bins in sub-grid i_{mr}
    for k_p from 1 to no. of points in the bin j_b
      $k_{p,i_{mr}j_b,\min} = k_p$ s.t. $P_{batt,i_{mr}j_bk_p} = \min(P_{batt,i_{mr}j_b})$
    End
  End
End

Definition of the set of points with minimum battery power consumption

$\mathrm{S} = \{(a_y, \delta_{sw}, P_{batt})_{i_{mr}j_bk_p} \text{s.t. } k_p = k_{p,i_{mr}j_b,\min}\}$

Computation of the minimum power envelope function

$P_{batt,\min} = \Lambda(a_y, \delta_{sw})$

a) The points $(a_{y,k}, \delta_{sw,k}, P_{batt,k})$ are split into N_{mr} macro-regions, identified by the index i_{mr}, based on $|a_y|$. As the density of points varies with $|a_y|$, it is convenient to apply grids with different resolutions based on $|a_y|$. The grid is finer where the density is higher, which is the case for low $|a_y|$ levels, at which the active systems do not bring as significant differentiation of the EV response as at high $|a_y|$. On the contrary, the grid is coarser where the density of points is lower, because this allows exclusion of points that belong to upper – and thus suboptimal – layers in terms of P_{batt}. The adoption of a high-resolution grid also where the points are sparse would yield an irregular minimum power envelope including outliers, i.e., samples that do not belong to the minimum power surface;
b) The macro-regions from a) are further partitioned into cells or bins, denoted by the index j_b, through a grid along the a_y- and δ_{sw}-axes;
c) For each bin j_b belonging to the macro-region i_{mr}, the point k_p that exhibits the lowest battery power, $P_{batt,i_{mr}j_b,min}$, with the corresponding $a_{y,i_{mr}j_b,min}$ and $\delta_{sw,i_{mr}j_b,min}$, is selected. The set of all extracted points across all bins is S;
d) A fitting based on a biharmonic interpolation function is performed on the points in S, to obtain the minimum power envelope function Λ, which establishes the relationship between a_y, δ_{sw}, and $P_{batt,min}$.

The same process was implemented also for the computation of the minimum power envelopes in terms of electric powertrain power losses, longitudinal tire slip power losses, and lateral tire slip power losses.

V. Results

A. Effect of Understeer Characteristic on Power Consumption

For the 2WD EV and each considered actuator configuration, indicated in the subplot titles, Fig. 9 reports:

- The energy-efficient UC, see Section IV, which is on the lowest edge of the minimum power envelope for each $|a_y|$.
- A carpet plot whose color map displays the battery power consumption increase, $P_{batt,inc}(|a_y|, |\delta_{sw}|)$, of the points located on the minimum power envelope w.r.t. the point on the energy-efficient UC at the same $|a_y|$:

$$P_{batt,inc}\ (|a_y|, |\delta_{sw}|) = \frac{P_{batt,\min}(|a_y|, |\delta_{sw}|) - P_{batt,opt}(|a_y|)}{P_{batt,opt}(|a_y|)}\ 100 \quad (30)$$

  where $P_{batt,opt}(|a_y|)$ is the battery power on the energy-efficient UC, and $P_{batt,\min}$ is the power consumption of the considered $(|a_y|, |\delta_{sw}|)$ point on the minimum power envelope. Hence, $P_{batt,inc}$ highlights the power consumption impact of the UC, i.e., the reference cornering behavior, and provides important chassis control design guidelines.

Moreover, for benchmarking, the subplots include:

- The UC, $\delta_{sw,ns}(a_y)$, corresponding to neutral steering:

$$\delta_{sw,ns} = k_{sw} \arctan\left(\frac{[a+b]\, a_y}{V^2}\right) \quad (31)$$

  where k_{sw} is the steering ratio. When the carpet plots extend below the level defined by $\delta_{sw,ns}(a_y)$, which occurs in Fig. 9(b), (d), (e)–(g), the EV is oversteering.
- The UC of the baseline version of the 2WD EV.

Fig. 9(a) shows that, in case of TV, the most efficient curve is generally close to the baseline, and corresponds to a less understeering behavior. The significant variation of P_{batt} and $P_{batt,inc}$ as a function of the M_z-induced variation of the level of understeer is highlighted in Fig. 10(a), which is a cross-section of Fig. 9(a) for $a_y = 3$, 5, and 7 m/s^2. Although neglected in the TV control design practice, the selection of the target UC, normally converted into a reference yaw rate map for feedback control, brings P_{batt} variations in excess of 10% across the $|a_y|$ range. RWS is characterized by a wide area of the carpet and gentle slopes of $P_{batt,inc}$, with P_{batt} variations up to ∼6%, see Figs. 9(b) and 10(b). The energy-efficient UC is predominantly on the top border of the area, which corresponds to the highest in-phase δ_r, and thus confirms the analysis based on (15)–(17). With the exception of the very high $|a_y|$ region, the active anti-roll moment distribution, see Fig. 9(c), corresponds to an optimal UC that is as close as possible – within the actuation constraints – to the neutral steering line, which minimizes $P_{loss,y}$.

For completeness, Figs. 11 and 12 report the cross sections of the minimum power envelopes in terms of $P_{loss,EP}$, $P_{loss,x}$, and $P_{loss,y}$, as a function of $|\delta_{sw}|$, for M_z and δ_r actuations, at the same lateral acceleration levels as in Fig. 10. The power levels in the right subplots of the figures, i.e., those showing $P_{loss,EP,norm}$, $P_{loss,x,norm}$, and $P_{loss,y,norm}$, are normalized as a percentage of $P_{batt,opt}(|a_y|)$, i.e., the battery power corresponding to the understeer characteristic minimizing the power consumption for the considered lateral acceleration. The observation of the results highlights the different significance of the power loss contributions. In fact, in both Figs. 11 and 12, for $|a_y| = 3$ m/s^2, $P_{loss,EP}$ and $P_{loss,y}$ tend to have similar magnitude, while $P_{loss,x}$ is lower by an order of magnitude. On

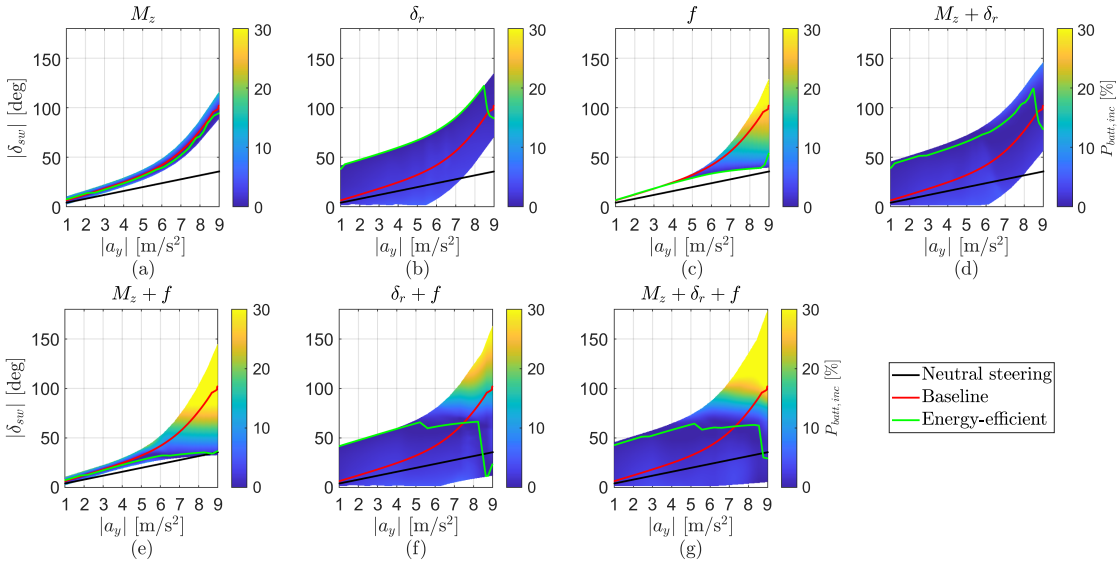

Fig. 9. Energy-efficient UCs, and carpet plots of the battery power increase, $P_{batt,inc}$, w.r.t. the baseline 2WD configuration, for the considered 2WD EV with the different chassis actuation suites, at zero a_x, $V = 100$ km/h, and $\mu_{\%} = 100\%$. The subplots also include the UCs for the neutral steering condition and the baseline 2WD configuration.

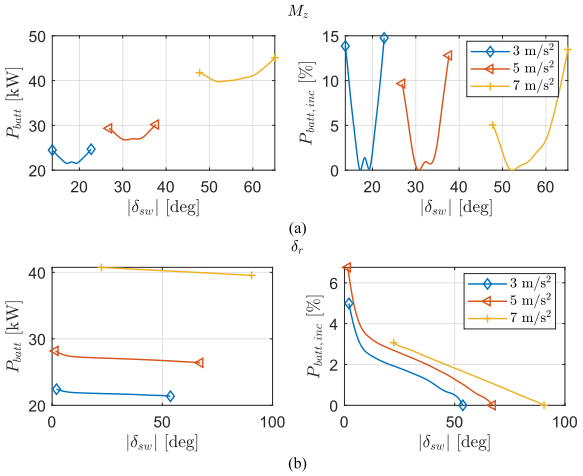

Fig. 10. Examples of P_{batt} and $P_{batt,inc}$ profiles as functions of $|\delta_{sw}|$, at $a_y = 3$, 5 and 7 m/s^2, extracted from the carpet plots for the M_z (Fig. 9(a)) and δ_r (Fig. 9(b)) actuations.

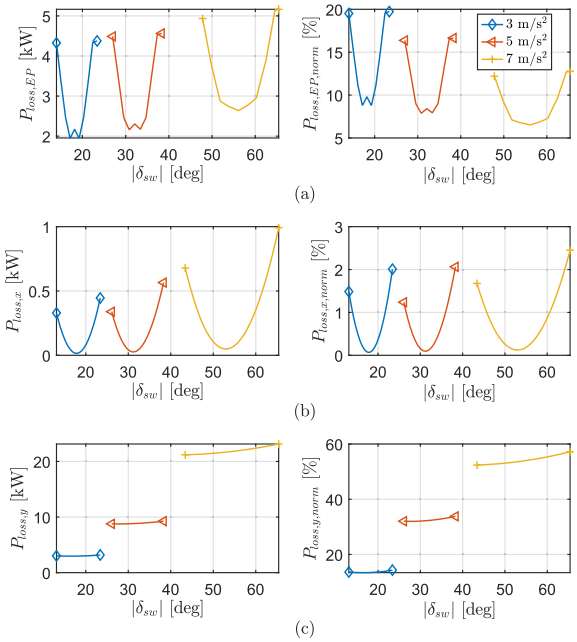

Fig. 11. Examples of power loss profiles as functions of $|\delta_{sw}|$, at $a_y = 3$, 5 and 7 m/s^2, extracted from the respective carpet plots of the minimum power envelopes for the M_z actuation.

the contrary, at 7 m/s^2, $P_{loss,y,norm}$ consistently exceeds 50%, which is at least four times higher than $P_{loss,EP}$, while $P_{loss,x}$ remains substantially negligible. The simultaneous observation of the individual power envelopes also enables the appreciation of the trade-offs associated with the achievement of the minimum battery power. For example, in Fig. 11, the powertrain power loss displays the same trend as the corresponding P_{batt}, with two local minima; in addition, $P_{loss,x}$ is minimized for a higher level of vehicle understeer than the optimal one in terms of $P_{loss,y}$. In Fig. 12, all proposed power loss contributions tend to decrease with increasing levels of vehicle understeer, which is consistent with the monotonically decreasing P_{batt} profile in Fig. 10(b).

The actuation combinations yield carpet plots and energy-efficient UCs that are a blend of those for the individual actuations. The dominant contribution up to medium $|a_y|$ is the one of RWS, if present, whereas the effect of AS or TV is more pronounced at higher $|a_y|$. In fact, in Fig. 9(d), (f), and (g), the energy-efficient UC starts close to the top edge of the carpet plot, similarly to Fig. 9(b), and then it progressively drifts towards the central region, or even to the bottom bound as in Fig. 9(f). Fig. 9(e) highlights the contributions of the two actuations, with M_z prevailing at low $|a_y|$, see the similarity of the energy-efficient UC with the one in Fig. 9(a) up to 4 m/s^2, which is followed by increasing significance of f at medium-to

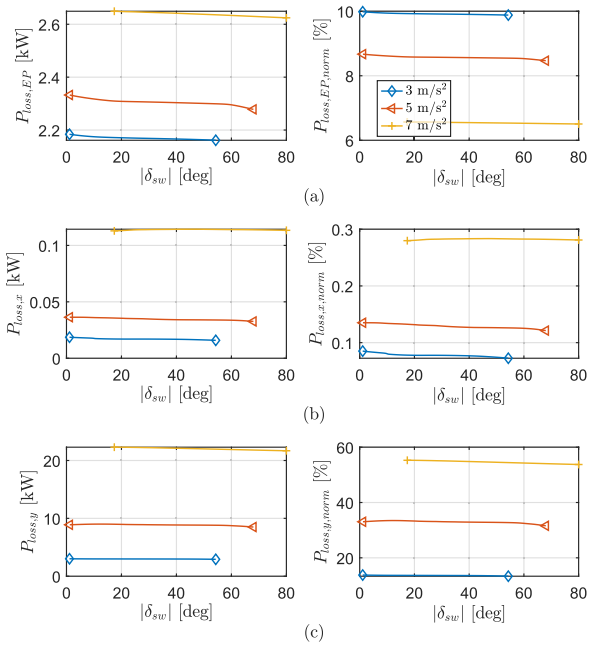

Fig. 12. Examples of power loss profiles as functions of $|\delta_{sw}|$, at $a_y = 3, 5$ and 7 m/s^2, extracted from the respective carpet plots of the minimum power envelopes for the δ_r actuation.

high $|a_y|$, with the final part of the optimal UC that is similar to the one for f on its own in Fig. 9(c).

The conclusion is that the selection of the reference cornering response is impactful already in the $|a_y|$ range (from 0 to 4 m/s^2) corresponding to normal driving. Results like those in Figs. 9 and 10 as well as in the following Section V-C allow the ICC designer to set the trade-off between: a) vehicle cornering, usually based on requirements deriving from the experience of each car maker, which would take priority in proximity of the cornering limit; and b) power consumption reduction, which could be the priority for low-to-medium lateral accelerations.

Some of the energy-efficient UCs in Fig. 9 clearly correspond to a sub-optimal or irregular cornering response performance. Nevertheless, the objective of the proposed routine based on carpet plots is to give the EV control designer a tool – which is not currently available – to achieve a desirable trade-off between energy efficiency and level of vehicle understeer.

B. Comparison of Power Consumption of Different Actuation Combinations Along Their Optimal Understeer Characteristics

This section compares the power consumption along the optimal UCs, to ascertain the efficiency potential of the different actuations. The analysis focuses on the battery power increase, $P_{batt,inc}$, expressed in percentage, relative to the configuration that is supposed to be the most efficient throughout the domain, namely the 4WD EV with $M_z + \delta_r + f$. For conciseness, only two testing conditions (TCs) covered by the simulations are discussed: TC1, i.e., the condition with zero a_x, $V = 100$ km/h, and $\mu_{\%} = 100\%$; and TC2, i.e., the same as TC1, apart from $a_x = 1.5$ m/s^2. It was verified that the trends do not change at

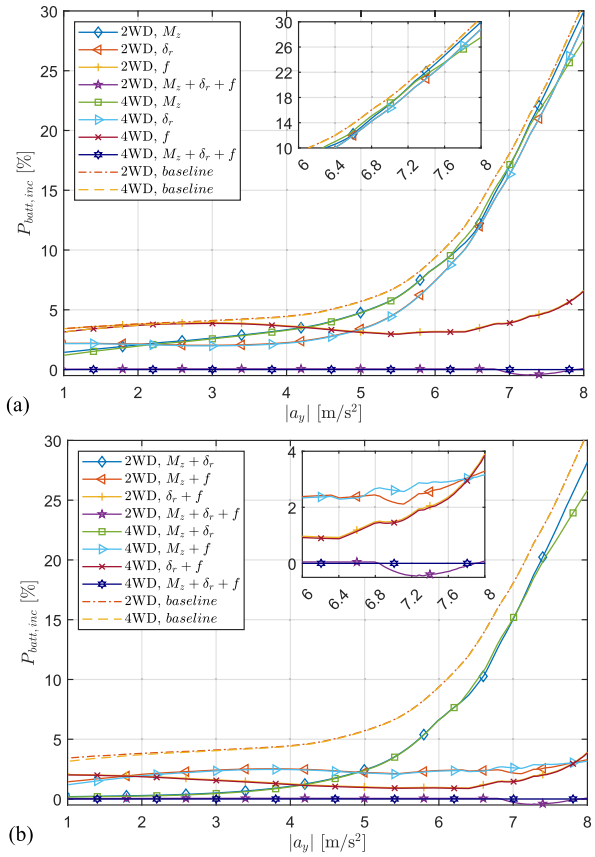

Fig. 13. Relative battery power increase, $P_{batt,inc}$ (in percentage), of the specified actuation configurations ((a) focuses on the single actuator configurations, while (b) focuses on the configurations with multiple actuators), w.r.t. the 4WD EV with $M_z + \delta_r + f$, at zero a_x, $V = 100$ km/h, and $\mu_{\%} = 100\%$. All configurations are operating on their energy-efficient UC.

different V and $\mu_{\%}$, and therefore the tests in TC1-2 are sufficient to convey the main conclusions.

For TC1, Fig. 13(a) shows the $P_{batt,inc}$ curves for the 2WD and 4WD configurations with single chassis actuation, while Fig. 13(b) includes the combinations with two actuations. Both figures also report the results of the baseline configurations, providing the top bound of the plots, and the two most over-actuated configurations (2WD and 4WD with $M_z + \delta_r + f$), which represent the bottom bounds. The main highlights are:

- The results of the 2WD and 4WD cases with the same chassis actuators are substantially coincident throughout the $|a_y|$ domain. This is caused by the rather low torque demand at zero a_x, for which, according to the $k_{d,opt,j}$ map in Fig. 6, the most efficient powertrain actuation implies the activation of a single powertrain – the rear one – per EV side, for most of the $|a_y|$ range. Hence, the 4WD EV tends to operate like a 2WD EV. This outcome is consistent with those from the available analyses for straight line EV operation, see [51] and [53].
- W.r.t. the single actuation configurations, TV and especially RWS are beneficial up to medium $|a_y|$, i.e., during normal vehicle operation, see Fig. 13(a), whereas the f actuation, which does not bring any advantage relative

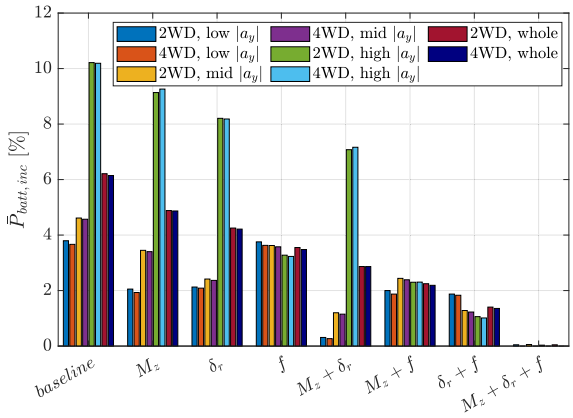

Fig. 14. Summary histograms showing the average battery power increase, $\bar{P}_{batt,inc}$, w.r.t. the 4WD EV with $M_z + \delta_r + f$, for bands of lateral acceleration, at zero a_x, $V = 100$ km/h, and $\mu_{\%} = 100\%$. All configurations are operating on their energy-efficient UC.

to the baselines at low $|a_y|$, becomes significantly more effective than M_z and δ_r in the nonlinear cornering region.

- At high $|a_y|$, see the views in the insets, the advantage of TV and RWS relative to the baselines is almost negligible.
- The trends in presence of multiple actuators (Fig. 13(b)) confirm those for the single actuator configurations, i.e., TV in conjunction with RWS is the most beneficial double actuation up to 4 m/s^2, but then is overtaken by the combinations including AS. Furthermore, the $\delta_r + f$ combination is generally more efficient than $M_z + f$.
- In presence of M_z actuation, the engagement of one of the front powertrains, occurring at $|a_y| \approx 6.5$ m/s^2 for $M_z + f$, and at $|a_y| \approx 6.8$ m/s^2 for $M_z + \delta_r + f$, implies a very marginal power consumption penalty for the 4WD cases, w.r.t. to the corresponding 2WD configurations. In fact, the optimization in (28) only accounts for the powertrain losses, and neglects dynamic effects such as the additional tire slips induced by the IWM engagement.

The previous results are summarized in Fig. 14, which displays the average values, $\bar{P}_{batt,inc}$, of battery power increase for three lateral acceleration bands (low, mid, and high $|a_y|$) of equal amplitude, as well as for the entire $|a_y|$ domain (referred to as 'whole', and corresponding to $|a_y|$ values from 1 to 8 m/s^2) in Fig. 13. The actuation combinations are sorted in descending $\bar{P}_{batt,inc}$ order (baseline, M_z, δ_r, f, $M_z + \delta_r$, $M_z + f$, $\delta_r + f$, and $M_z + \delta_r + f$) across the whole lateral acceleration range (with values amounting to 6.15%, 4.87%, 4.22%, 3.48%, 2.86%, 2.19%, 1.36%, and zero, for the respective 4WD configurations), while the ranking is different if the individual $|a_y|$ ranges are considered. For example, at low $|a_y|$, the ascending efficiency ranking order of the 4WD cases is baseline (with 3.67% $\bar{P}_{batt,inc}$), f (3.63%), δ_r (2.09%), M_z (1.93%), $M_z + f$ (1.87%), $\delta_r + f$ (1.83%), $M_z + \delta_r$ (0.27%), and $M_z + \delta_r + f$, while at high $|a_y|$ the order is baseline (10.19%), M_z (9.26%), δ_r (8.18%), $M_z + \delta_r$ (7.16%), $M_z + f$ (2.30%), $\delta_r + f$ (1.01%), and $M_z + \delta_r + f$.

The TC2 results are reported in Fig. 15(a) for the single actuation cases, and Fig. 15(b) for the double actuator configurations,

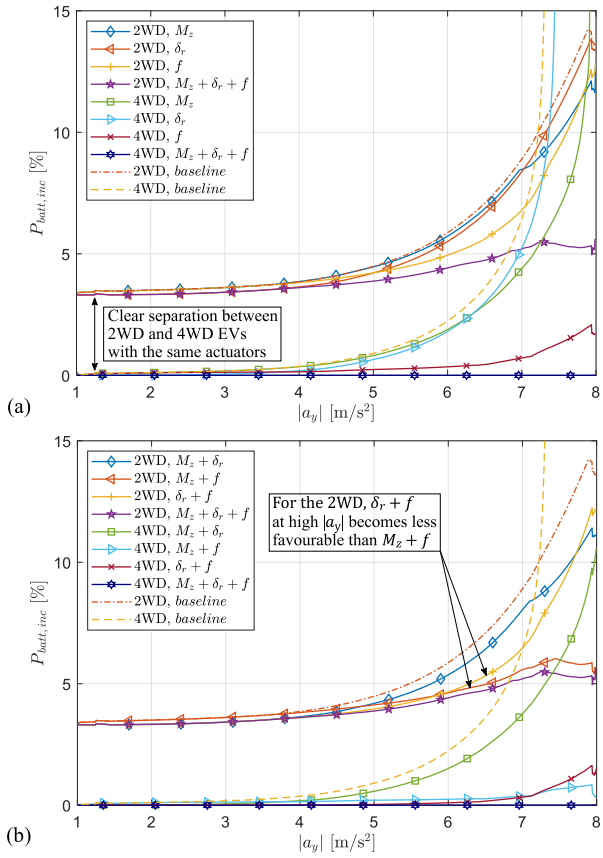

Fig. 15. $P_{batt,inc}$ for the specified actuation configurations ((a) focuses on the single actuator configurations, while (b) focuses on the configurations with multiple actuators), w.r.t. the 4WD EV with $M_z + \delta_r + f$, for $a_x = 1.5$ m/s^2, $V = 100$ km/h, and $\mu_{\%} = 100\%$. All configurations are operating on their energy-efficient UC.

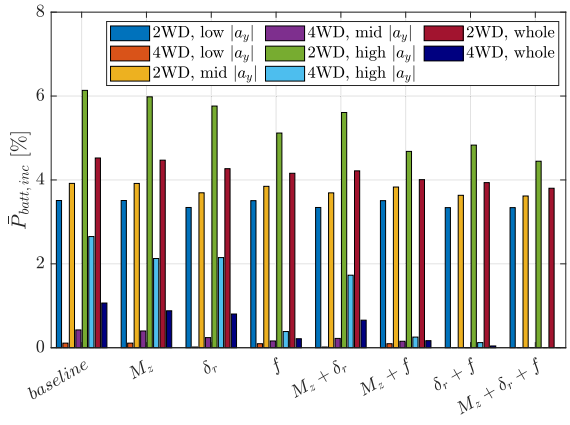

Fig. 16. Summary histograms showing the average power increase, $\bar{P}_{batt,inc}$, w.r.t. the 4WD EV with $M_z + \delta_r + f$, for bands of lateral acceleration, at $a_x = 1.5$ m/s^2, $V = 100$ km/h, and $\mu_{\%} = 100\%$. All configurations are operating on their energy-efficient UC.

while summary bar plots are in Fig. 16. For consistency, the line styles associated with each actuation configuration are the same as for TC1. Nevertheless, the shape of the resulting graphs and the rankings are radically different. The main observations are:

- The additional traction force w.r.t. the condition with zero a_x translates into a very net separation between the 2WD

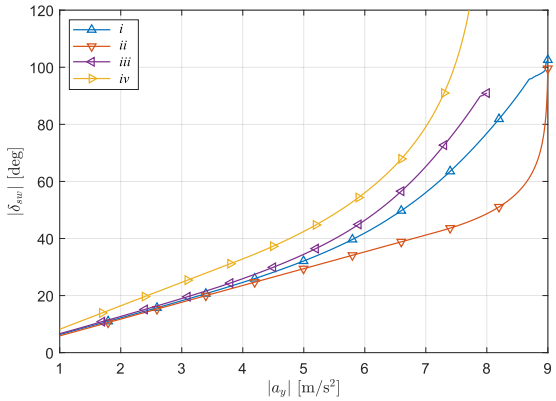

Fig. 17. Selected UCs for $V = 100$ km/h and $\mu_{\%} = 100\%$: (*i*) characteristic of the baseline 2WD EV at zero a_x; (*ii*) sport-oriented characteristic at zero a_x, i.e., with reduced understeer w.r.t. *i*; (*iii*) characteristic of the baseline 2WD EV at $a_x = 1.5$ m/s^2; and (*iv*) stability-oriented characteristic at $a_x = 1.5$ m/s^2, i.e., with increased understeer w.r.t. *iii*.

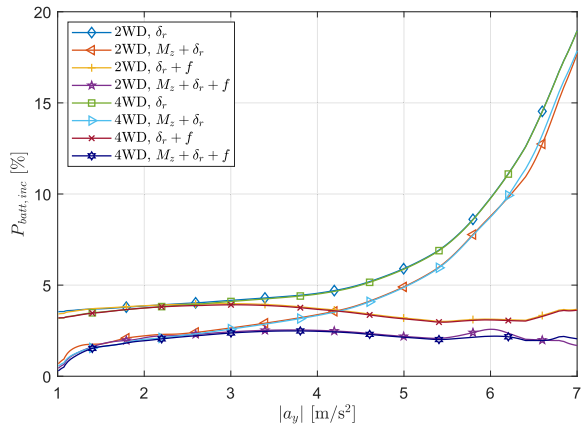

Fig. 18. $P_{batt,inc}$ for the considered actuation configurations along characteristic *ii* in Fig. 17, for zero a_x, $V = 100$ km/h, and $\mu_{\%} = 100\%$, w.r.t. the 4WD $M_z + \delta_r + f$ configuration on its energy-efficient UC.

and 4WD EVs with the same actuators, see also the comment in Fig. 15(a). In fact, at rather high torque, it is considerably more efficient to deliver torque also through the front motors, which is consistent with the results in [51] and [53], obtained for zero a_y conditions. This is highlighted by the significantly larger $\bar{P}_{batt,inc}$ values for the 2WD EV configurations in all $|a_y|$ ranges, corresponding to an average 3.5% battery power increase w.r.t. the corresponding 4WD EV.

- AS still guarantees significant advantages at high $|a_y|$, especially together with the variable longitudinal torque distribution of the 4WD cases, e.g., $\bar{P}_{batt,inc}$ amounts to 2.65% for the 4WD baseline configuration, and 0.39% for the f actuation case.
- Although the general trends are the same as for zero a_x conditions, the effect of TV and RWS at low $|a_y|$, which was evident in TC1, is rather negligible in TC2. In fact, for the 2WD case, $\bar{P}_{batt,inc}$ amounts to 3.51% for the baseline configuration, 3.51% for M_z, and 3.34% for δ_r.
- In Fig. 16 the trends are similar to those for zero a_x when considering the entire $|a_y|$ domain. On the contrary,

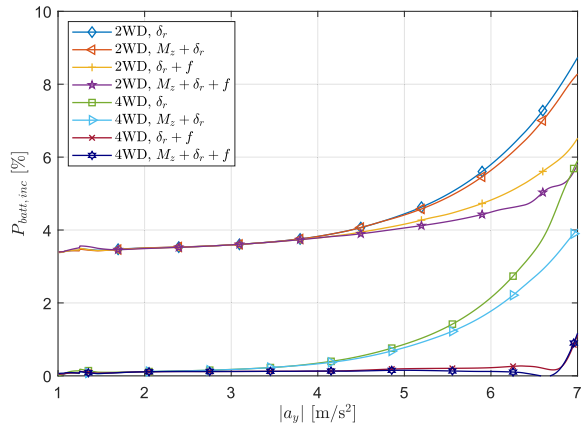

Fig. 19. $P_{batt,inc}$ for the considered actuation configurations along UC *iv* in Fig. 17, for $a_x = 1.5$ m/s^2, $V = 100$ km/h, and $\mu_{\%} = 100\%$, w.r.t. the 4WD $M_z + \delta_r + f$ configuration on its energy-efficient UC.

the rankings differ in the low and medium $|a_y|$ intervals for both the 2WD and 4WD cases, and, for the 2WD configurations, also in the high $|a_y|$ range. In fact, in contrast with the results for zero a_x, in the low and medium $|a_y|$ ranges, $M_z + \delta_r$ is as efficient as or marginally less efficient than $\delta_r + f$, which holds both for the 2WD and 4WD cases. Across the whole range, the cases with AS, i.e., $M_z + f$ and $\delta_r + f$, are still more efficient, with $\bar{P}_{batt,inc}$ respectively amounting to 0.17% and 0.04% for the 4WD configurations (4.01% and 3.94% for the respective 2WD cases), than $M_z + \delta_r$, having a $\bar{P}_{batt,inc}$ value of 0.66% for the 4WD EV (4.22% for the 2WD). However, as the lateral acceleration limit is approached, for the 2WD EV, which cannot benefit from the powertrain efficiency enhancement of the optimal front-to-total torque distribution, the $\delta_r + f$ actuation, with 4.83% $\bar{P}_{batt,inc}$ at high $|a_y|$, becomes less favorable than $M_z + f$, corresponding to 4.68% $\bar{P}_{batt,inc}$ in the same conditions, thus changing the ranking of the actuators w.r.t. the zero a_x condition.

C. Energy-Efficient Cornering Response and Control Allocation

Reference understeer characteristics – The previous analyses focused on the optimal UCs, and the power consumption associated with the different actuator combinations. However, some of the energy-efficient UCs in Fig. 9 show an irregular behavior, which may be unacceptable from the drivability and vehicle dynamics viewpoints, and prove difficult to smoothen in practice. Hence, for the implementation, it could be practical to consider energy efficiency only in the CA layer, which is the current state-of-the-art of chassis control, while the reference cornering response, defined by the UCs, may be selected based on other considerations, e.g., to target desirable vehicle dynamics. Therefore, for each combination of chassis actuators, this section evaluates: a) the penalty of considering energy efficiency only in the CA layer, while using reference UCs that are desirable in terms of cornering response, but are not conceived for energy

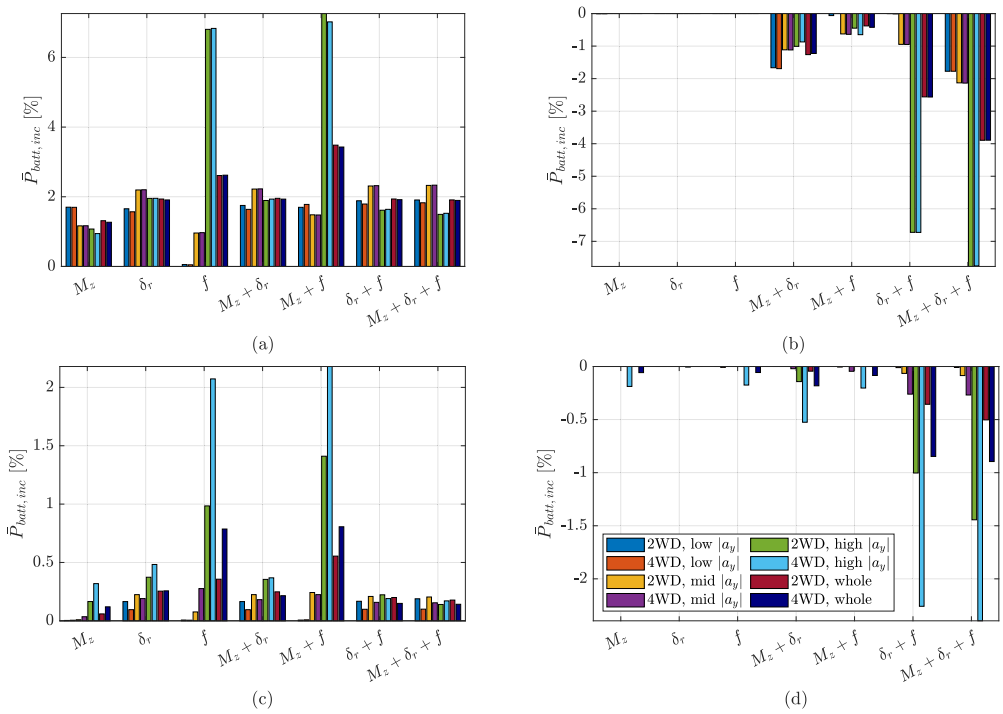

Fig. 20. Summary plots for $V = 100$ km/h and $\mu_{\%} = 100\%$. (a) and (b): average battery power increase, $\bar{P}_{batt,inc}$, while tracking UC *i*, for zero a_x; (c) and (d): $\bar{P}_{batt,inc}$ while tracking characteristic *iii* in Fig. 17, for $a_x = 1.5$ m/s^2. In (a) and (c) the $\bar{P}_{batt,inc}$ value for each set-up is relative to the corresponding 2WD or 4WD configuration tracking the respective energy-efficient UC. In (b) and (d) the $\bar{P}_{batt,inc}$ value for each set-up is relative to the 2WD or 4WD baseline EV.

efficiency; and b) the energy consumption benefits of optimal CA w.r.t. the baseline EV operation.

For $V = 100$ km/h, the consumption is assessed along the minimum power envelopes of the controlled configurations in Section IV, for the points corresponding to the UCs of the 2WD baseline EV at $a_x = 0$ and 1.5 m/s^2, respectively *i* and *iii* in Fig. 17, and two selected realistic (from the vehicle dynamics perspective) characteristics, indicated as *ii* and *iv*, respectively less and more understeering than *i* and *iii*. Characteristic *ii* corresponds to the one of a typical sport mode, selectable by the driver, see [3], while *iv* resembles the one of a typical stability mode. As *ii* and *iv* are not entirely feasible through some of the actuation configurations and specified maximum levels of control effort, e.g., this is the case for TV and AS on their own, the results are reported only for the actuations that can achieve the characteristics across the whole a_y range.

Comparison with the most over-actuated EV configuration tracking its energy-efficient understeer characteristic – For characteristic *ii* tracked by the indicated chassis actuation configurations, Fig. 18 plots the battery power increase, $P_{batt,inc}$, w.r.t. the most over-actuated 4WD configuration, $M_z + \delta_r + f$, operating on its energy-efficient UC. Given the suboptimality of *ii*, all curves show power increments throughout the domain. For example, along *ii*, the complete set of actuators, i.e., $M_z + \delta_r + f$, brings a power consumption increase that remains within a 2% bound w.r.t. to its use along the energy-efficient UC. The other trends are aligned with those in Fig. 13: a) the curves of the 2WD and 4WD configurations are substantially the same across the $|a_y|$ domain; b) at low $|a_y|$, two sets of curves are visible, depending on the presence or absence of M_z actuation, i.e., TV is the most effective chassis control method up to ∼4 m/s^2; and c) the effect of f is the prevalent one at medium-to-high $|a_y|$ (i.e., ranging from the end of the linear cornering response region to close-to-limit handling conditions), where the presence or absence of AS determines two distinct trends of $P_{batt,inc}$, which differ from each other by ∼15% at $|a_y| = 7$ m/s^2.

Fig. 19 refers to $a_x = 1.5$ m/s^2, with the different actuation configurations tracking UC *iv*. The trends and power increase values are very similar to those in Fig. 15. This indicates a negligible effect of the UC on the results, which show: a) the very clear separation between the 2WD and 4WD curves across the a_y domain, with a power increase by ∼3% for the 2WD case; and b) the benefit of AS actuation at medium-to-high $|a_y|$, which brings ∼3% consumption reduction for $a_y = 7$ m/s^2.

Summary plots – As a summary, for $V = 100$ km/h and the three defined lateral acceleration intervals, as well as for the whole $|a_y|$ range, Fig. 20 reports $\bar{P}_{batt,inc}$ for the considered actuation configurations using optimal CA (i.e., by operating the actuators on the minimum power envelope) and tracking:

- The baseline UC *i* in Fig. 17, where the power variation is computed w.r.t. the corresponding 2WD or 4WD actuation configuration, along its energy-efficient UC, for EV operation at zero a_x (subplot (a) of Fig. 20). Hence, the results indicate the benefit of the optimal UCs, which, on average, amounts to ∼2%, with peaks in excess of 6% for f and $f + M_z$ for the 2WD and 4WD EVs at high $|a_y|$.
- The baseline UC *i*, where the battery power variation is computed w.r.t. the baseline 2WD or 4WD configuration,

for zero a_x (subplot (b)). The negative values of $\bar{P}_{batt,inc}$ indicate the power consumption reduction brought by optimal CA, which reaches its peak – in excess of 7% – for $\delta_r + M_z$ and $f + \delta_r + M_z$ in the high $|a_y|$ range.

- The UC *iii*, where $\bar{P}_{batt,inc}$ is computed w.r.t. the same 2WD or 4WD actuation configuration along its energy-efficient UC, for $a_x = 1.5$ m/s^2 (subplot (c)). The selection of the energy-efficient cornering response brings an average consumption reduction that remains below 1%, with peaks in excess of 2% for f and $M_z + f$ at high $|a_y|$. Such savings are less than half than those at zero a_x. Based on the comparison of subplots (a) and (c), the appropriate UC selection is particularly important at low torque demand, and especially in presence of AS actuation, which is directly correlated to the lateral tire slip power loss.
- The UC *iii*, where $P_{batt,inc}$ is computed w.r.t. the baseline 2WD or 4WD configuration, at $a_x = 1.5$ m/s^2 (subplot (d)). In most cases the power consumption reduction is less than 0.5%, with peaks over 2% for $\delta_r + f$ and $M_z + \delta_r + f$. The comparison of the results in subplots (c) and (d) shows that also in non-zero a_x conditions the benefits of the energy-efficient UCs and CA have comparable magnitude, and therefore the two techniques should be concurrently implemented in the next generation of multi-actuated EVs.

VI. Conclusion

The paper discussed the effect of the control of the front-to-total wheel torque distribution, torque-vectoring (TV, corresponding to M_z control), rear-wheel steering (RWS, implying δ_r control), and front-to-total anti-roll moment distribution through active suspension (AS) actuation (f control), on the power consumption of an electric vehicle (EV) with in-wheel motors, operating in quasi-steady-state cornering and traction. A simulation campaign was used to find the energy-efficient understeer characteristics, and the energy-efficient control allocations to achieve given levels of vehicle understeer. Differently from the available integrated chassis control literature, the obtained results are independent from the constraints or specificities of any controller implementation.

For the specific EV, the main conclusions are:

- The front-to-total wheel torque distribution does not have any impact on the power consumption in conditions of zero longitudinal acceleration (a_x), i.e., on average the benefit of 4WD operation amounts to $<0.1\%$ across the lateral acceleration (a_y) domain. In fact, at low torque demand, it is more efficient to operate a single powertrain per EV side, i.e., the energy-efficient 4WD EV works as a 2WD EV.
- For non-zero a_x, when the high torque demand favors the simultaneous use of the front and rear powertrains, the front-to-total torque distribution has the highest impact on power consumption, among the considered actuations. This results in an average 3.5% benefit of the 4WD configurations w.r.t. the corresponding 2WD EV.
- The front-to-total anti-roll moment distribution is ineffective at low $|a_y|$, but has significant impact at medium-to-high $|a_y|$, yielding, in such conditions, power consumption benefits w.r.t. TV and RWS.
- TV and RWS are effective up to medium $|a_y|$, especially for low torque demand; beyond the linear cornering range, their consumption benefit is subject to significant reduction.
- At zero a_x, the ranking of the considered chassis actuation configurations, from the one with the highest power demand to the most efficient one, across the whole lateral acceleration range, is: baseline, M_z, δ_r, f, $M_z + \delta_r$, $M_z + f$, $\delta_r + f$, and $M_z + \delta_r + f$. In traction, for both the 2WD and 4WD cases, the actuation ranking for the whole lateral acceleration band remains the same as for zero a_x, while exceptions occur in the individual lateral acceleration ranges. For example, for the 2WD configuration at high lateral accelerations, $\delta_r + f$ is less favorable than $M_z + f$.
- The selection of the cornering response, corresponding to the reference understeer characteristic, has a major impact on the battery power consumption. For example, the power consumption increment for the EV operating along its baseline understeer characteristic and with optimal control allocation – in comparison with the same EV configuration working on its energy-efficient understeer characteristic – amounts to $\sim$2% across the lateral acceleration range at zero a_x, with peaks in excess of 6% for f and $f + M_z$ for the 2WD and 4WD EVs at high $|a_y|$. On average, the optimal understeer characteristic has similar impact w.r.t. the adoption of optimal control allocation algorithms.

References

[1] "Global EV sales for 2022," Jan. 2023. [Online]. Available: https://www.ev-volumes.com/

[2] L. De Novellis, A. Sorniotti, and P. Gruber, "Optimal wheel torque distribution for a four-wheel-drive fully electric vehicle," *SAE Int. J. Passenger Cars - Mech. Syst.*, vol. 6, no. 1, pp. 128–136, Apr. 2013.

[3] L. De Novellis, A. Sorniotti, and P. Gruber, "Driving modes for designing the cornering response of fully electric vehicles with multiple motors," *Mech. Syst. Signal Process.*, vol. 64–65, pp. 1–15, Dec. 2015.

[4] M. Jonasson, J. Andreasson, S. Solyom, B. Jacobson, and A. Stensson Trigell, "Utilization of actuators to improve vehicle stability at the limit: From hydraulic brakes toward electric propulsion," *J. Dyn. Syst., Meas. Control*, vol. 133, no. 5, Sep. 2011, Art. no. 051003.

[5] J. Kang, J. Yoo, and K. Yi, "Driving control algorithm for maneuverability, lateral stability, and rollover prevention of 4WD electric vehicles with independently driven front and rear wheels," *IEEE Trans. Veh. Technol.*, vol. 60, no. 7, pp. 2987–3001, Sep. 2011.

[6] A. Pennycott, L. D. Novellis, P. Gruber, and A. Sorniotti, "Sources of power loss during torque-vectoring for fully electric vehicles," *Int. J. Veh. Des.*, vol. 67, no. 2, 2015, Art. no. 157.

[7] X. Yuan and J. Wang, "Torque distribution strategy for a front- and rear-wheel-driven electric vehicle," *IEEE Trans. Veh. Technol.*, vol. 61, no. 8, pp. 3365–3374, Oct. 2012.

[8] Y. Chen and J. Wang, "Adaptive energy-efficient control allocation for planar motion control of over-actuated electric ground vehicles," *IEEE Trans. Control Syst. Technol.*, vol. 22, no. 4, pp. 1362–1373, Jul. 2014.

[9] P. Sun, A. Stensson Trigell, L. Drugge, and J. Jerrelind, "Energy-efficient direct yaw moment control for in-wheel motor electric vehicles utilising motor efficiency maps," *Energies*, vol. 13, no. 3, Jan. 2020, Art. no. 593.

[10] L. De Novellis, A. Sorniotti, and P. Gruber, "Wheel torque distribution criteria for electric vehicles with torque-vectoring differentials," *IEEE Trans. Veh. Technol.*, vol. 63, no. 4, pp. 1593–1602, May 2014.

[11] T. Kobayashi, E. Katsuyama, H. Sugiura, E. Ono, and M. Yamamoto, "Efficient direct yaw moment control: Tyre slip power loss minimisation for four-independent wheel drive vehicle," *Veh. Syst. Dyn.*, vol. 56, no. 5, pp. 719–733, May 2018.
[12] Y. Suzuki, Y. Kano, and M. Abe, "A study on tyre force distribution controls for full drive-by-wire electric vehicle," *Veh. Syst. Dyn.*, vol. 52, no. sup1, pp. 235–250, May 2014.
[13] T. Kobayashi, E. Katsuyama, H. Sugiura, E. Ono, and M. Yamamoto, "Efficient direct yaw moment control during acceleration and deceleration while turning," SAE Tech. Paper 2016-01-1674, Apr. 2016.
[14] H. Fujimoto and S. Harada, "Model-based range extension control system for electric vehicles with front and rear driving–braking force distributions," *IEEE Trans. Ind. Electron.*, vol. 62, no. 5, pp. 3245–3254, May 2015.
[15] G. De Filippis, B. Lenzo, A. Sorniotti, P. Gruber, and W. De Nijs, "Energy-efficient torque-vectoring control of electric vehicles with multiple drivetrains," *IEEE Trans. Veh. Technol.*, vol. 67, no. 6, pp. 4702–4715, Jun. 2018.
[16] N. Guo, X. Zhang, Y. Zou, B. Lenzo, T. Zhang, and D. Göhlich, "A fast model predictive control allocation of distributed drive electric vehicles for tire slip energy saving with stability constraints," *Control Eng. Pract.*, vol. 102, Sep. 2020, Art. no. 104554.
[17] X. Hu, H. Chen, Z. Li, and P. Wang, "An energy-saving torque vectoring control strategy for electric vehicles considering handling stability under extreme conditions," *IEEE Trans. Veh. Technol.*, vol. 69, no. 10, pp. 10787–10796, Oct. 2020.
[18] B. Zhao, N. Xu, H. Chen, K. Guo, and Y. Huang, "Design and experimental evaluations on energy-efficient control for 4WIMD-EVs considering tire slip energy," *IEEE Trans. Veh. Technol.*, vol. 69, no. 12, pp. 14631–14644, Dec. 2020.
[19] A. Singh, A. Kumar, R. Chaudhary, and R. C. Singh, "Study of 4 wheel steering systems to reduce turning radius and increase stability," in *Proc. Int. Conf. Adv. Res. Innov.*, 2014, pp. 96–102.
[20] G. Cui, X. Shang, Z. Li, F. Ning, and X. Wu, "Lateral stability control of four-wheel steering vehicles," in *Proc. 3rd Conf. Veh. Control Intell.*, 2019, pp. 1–5.
[21] N. Hamzah, M. K. Aripin, Y. M. Sam, H. Selamat, and M. F. Ismail, "Yaw stability improvement for four-wheel active steering vehicle using sliding mode control," in *Proc. IEEE 8th Int. Colloq. Signal Process. Appl.*, 2012, pp. 127–132.
[22] F. Wang and Y. Chen, "Hierarchical input-output decoupling control for vehicle rollover mitigation," in *Proc. ASME Dyn. Syst. Control Conf.*, 2018, Paper V001T09A005.
[23] W. Shufeng and L. Huashi, "Integrated rear wheel steering angle and yaw moment optimal control of four-wheel-steering vehicle," in *Proc. Chin. Control Decis. Conf.*, 2010, pp. 2490–2493.
[24] B. Yang, M. Wan, and Q. Sun, "Control strategy for four-wheel steering vehicle handling stability based on partial decoupling design," in *Proc. 3rd Int. Joint Conf. Comput. Sci. Optim.*, 2010, pp. 265–267.
[25] J. Edrén, M. Jonasson, J. Jerrelind, A. Stensson Trigell, and L. Drugge, "Energy efficient cornering using over-actuation," *Mechatronics*, vol. 59, pp. 69–81, May 2019.
[26] F. Wang, P. Xu, A. Li, and Y. Chen, "Energy optimization of lateral motions for autonomous ground vehicles with four-wheel steering control," in *Proc. ASME Dyn. Syst. Control Conf.*, 2019, Paper V001T08A002.
[27] S. Bhat, M. Davari, and M. Nybacka, "Study on energy loss due to cornering resistance in over-actuated vehicles using optimal control," *SAE Int. J. Veh. Dyn. Stability NVH*, vol. 1, no. 2, pp. 263–269, 2017.
[28] F. Xu, X. Liu, W. Chen, and C. Zhou, "Dynamic switch control of steering modes for four wheel independent steering rescue vehicle," *IEEE Access*, vol. 7, pp. 135595–135605, 2019.
[29] J. Na, Y. Huang, X. Wu, G. Gao, G. Herrmann, and J. Z. Jiang, "Active adaptive estimation and control for vehicle suspensions with prescribed performance," *IEEE Trans. Control Syst. Technol.*, vol. 26, no. 6, pp. 2063–2077, Nov. 2018.
[30] M. C. Chen, W.-Y. Wang, S. F. Su, and Y. H. Chien, "Robust T-S fuzzy-neural control of uncertain active suspension systems," *Int. J. Fuzzy Syst.*, vol. 12, no. 4, pp. 321–329, Dec. 2010.
[31] M. Ricco et al., "On the model-based design of front-to-total anti-roll moment distribution controllers for yaw rate tracking," *Veh. Syst. Dyn.*, vol. 60, pp. 569–596, Oct. 2020.
[32] M. O. Bodie and A. Hac, "Closed loop yaw control of vehicles using magneto-rheological dampers," SAE Tech. Paper 2000-01-0107, Mar. 2000.
[33] P. H. Cronjé and P. S. Els, "Improving off-road vehicle handling using an active anti-roll bar," *J. Terramechanics*, vol. 47, no. 3, pp. 179–189, Jun. 2010.
[34] G. Long, F. Ding, N. Zhang, J. Zhang, and A. Qin, "Regenerative active suspension system with residual energy for in-wheel motor driven electric vehicle," *Appl. Energy*, vol. 260, Feb. 2020, Art. no. 114180.
[35] A. A. Aldair and W. J. Wang, "The energy regeneration of electromagnetic energy saving active suspension in full vehicle with neurofuzzy controller," *Int. J. Artif. Intell. Appl.*, vol. 2, no. 2, pp. 32–43, Apr. 2011.
[36] L. Chen, D. Shi, R. Wang, and H. Zhou, "Energy conservation analysis and control of hybrid active semiactive suspension with three regulating damping levels," *Shock Vib.*, vol. 2016, 2016, Art. no. 6196542.
[37] P. Sun, A. Stensson Trigell, L. Drugge, J. Jerrelind, and M. Jonasson, "Exploring the potential of camber control to improve vehicles' energy efficiency during cornering," *Energies*, vol. 11, no. 4, Mar. 2018, Art. no. 724.
[38] K. Shimada and Y. Shibahata, "Comparison of three active chassis control methods for stabilizing yaw moments," SAE Tech. Paper 940870, Mar. 1994.
[39] A. Hac and M. O. Bodie, "Improvements in vehicle handling through integrated control of chassis systems," *Int. J. Veh. Des.*, vol. 29, no. 1/2, 2004, Art. no. 23.
[40] A. H. Ahangarnejad, S. Melzi, and M. Ahmadian, "Integrated vehicle dynamics system through coordinating active aerodynamics control, active rear steering, torque vectoring and hydraulically interconnected suspension," *Int. J. Automot. Technol.*, vol. 20, no. 5, pp. 903–915, Oct. 2019.
[41] V. Mazzilli et al., "Integrated chassis control: Classification, analysis and future trends," *Annu. Rev. Control*, vol. 51, pp. 172–205, 2021.
[42] B. Li, H. Du, W. Li, and B. Zhang, "Integrated dynamics control and energy efficiency optimization for overactuated electric vehicles," *Asian J. Control*, vol. 20, no. 6, pp. 1–15, 2018.
[43] L. Li, S. Coskun, R. Langari, and J. Xi, "Incorporated vehicle lateral control strategy for stability and enhanced energy saving in distributed drive hybrid bus," *Appl. Soft Comput.*, vol. 111, 2021, Art. no. 107617.
[44] B. Shyrokau, D. Wang, D. Savitski, K. Hoepping, and V. Ivanov, "Vehicle motion control with subsystem prioritization," *Mechatronics*, vol. 30, pp. 297–315, Sep. 2015.
[45] Y. Li, J. Zhang, C. Lv, and Y. Yuan, "Coordinated control of the steering system and the distributed motors for comprehensive optimization of the dynamics performance and the energy consumption of an electric vehicle," *Proc. Inst. Mech. Engineers, Part D: J. Automobile Eng.*, vol. 231, no. 12, pp. 1605–1626, 2017.
[46] H. Sumiya and H. Fujimoto, "Electric vehicle range extension control system based on front- and rear-wheel sideslip angle and left- and right-motor torque distribution," *IEEJ Trans. Ind. Appl.*, vol. 132, no. 3, pp. 308–314, Mar. 2012.
[47] C. Jing, H. Shu, R. Shu, and Y. Song, "Integrated control of electric vehicles based on active front steering and model predictive control," *Control Eng. Pract.*, vol. 121, Apr. 2022, Art. no. 105066.
[48] M. Dalboni et al., "Nonlinear model predictive control for integrated energy-efficient torque-vectoring and anti-roll moment distribution," *IEEE/ASME Trans. Mechatron.*, vol. 26, no. 3, pp. 1212–1224, Jun. 2021.
[49] C. Chatzikomis et al., "An energy-efficient torque-vectoring algorithm for electric vehicles with multiple motors," *Mech. Syst. Signal Process.*, vol. 128, pp. 655–673, Aug. 2019.
[50] T. Kobayashi, E. Katsuyama, H. Sugiura, Y. Hattori, E. Ono, and M. Yamamoto, "Theoretical analysis of tyre slip power dissipation mechanism using brush model," *Veh. Syst. Dyn.*, vol. 58, no. 8, pp. 1242–1256, 2020.
[51] B. Lenzo et al., "Torque distribution strategies for energy-efficient electric vehicles with multiple drivetrains," *J. Dyn. Syst., Meas. Control*, vol. 139, no. 12, pp. 1–13, Dec. 2017.
[52] W. F. Milliken and D. L. Milliken, *Race Car Vehicle Dynamics*. Warrendale, PA, USA: SAE, 1994.
[53] A. M. Dizqah, B. Lenzo, A. Sorniotti, P. Gruber, S. Fallah, and J. De Smet, "A fast and parametric torque distribution strategy for four-wheel-drive energy-efficient electric vehicles," *IEEE Trans. Ind. Electron.*, vol. 63, no. 7, pp. 4367–4376, Jul. 2016.

Matteo Dalboni received the M.Sc. degree in mechanical engineering and the Ph.D. degree in information technology from the University of Parma, Parma, Italy, in 2017 and 2021, respectively. He is currently a Research Assistant with the Power Electronics Group with the same university. His research interests include vehicle dynamics and control (with focus on fully electric vehicles with independent drives and multiple actuations), and control of power electronics converters.

Gil Martins received the M.Eng. degree in automotive engineering from the University of Surrey, Guildford, U.K., in 2020. He is a Vehicle Development Engineer with Gordon Murray Advanced Engineering, developing products such as T.50 and T.33. His research interests include vehicle dynamics and aerothermal management.

Davide Tavernini received the M.Sc. degree in mechanical engineering and Ph.D. degree in dynamics and design of mechanical systems from the University of Padova, Padua, Italy, in 2010 and 2014. During his Ph.D. he was part of the Motorcycle Dynamics Research Group. He is a Senior Lecturer in advanced vehicle engineering with the University of Surrey, Guildford, U.K. His research interests include vehicle dynamics modeling, control and state estimation, applied to over-actuated vehicles.

Umberto Montanaro received the M.Sc. degree in computer science engineering and the Ph.D. degrees in control engineering and mechanical engineering from the University of Naples Federico II, Naples, Italy, in 2005, 2009, and 2016, respectively. He is currently a Senior Lecturer of control engineering and autonomous systems with the University of Surrey, Guildford, U.K. His research interests include adaptive control, and control of piecewise affine mechatronic and automotive systems.

Alessandro Soldati is a Researcher with the University of Parma, Parma, Italy, in the fields of power electronics and energy engineering. In 2017 he cofounded the spin-off company eDriveLAB for vehicle electrification, and was a Visiting Scholar with Aalborg University, Aalborg, Denmark. In 2018, he discussed his Ph.D. thesis about an innovative gate driver that can boost lifetime of power electronics devices. He was the Principal Investigator of a project funded by Interreg ADRION. He is author of 38 scientific peer-reviewed papers and co-inventor of six granted patents.

Carlo Concari (Member, IEEE) received the Ph.D. degree in information technology from the University of Parma, Parma, Italy, in 2006. He is currently an Associate Professor with the Department of Engineering and Architecture, University of Parma. His research interests include power electronics, drive control, electric propulsion, static power converters, and electric machines diagnostics.

Miguel Dhaens received the M.Sc. degree in electromechanical engineering from KIH, Ostend, Belgium. He was an Engineering Manager with the Global Research Ride Performance Team, Tenneco, Belgium, and responsible for defining the research road map and coordinating the global research activities of Tenneco's Ride Performance business. He is currently the CEO of Heronsports, Lommel, Belgium, a start-up company focusing on innovative suspension and steering concepts.

Aldo Sorniotti (Member, IEEE) received the M.Sc. degree in mechanical engineering and the Ph.D. degree in applied mechanics from the Politecnico di Torino, Turin, Italy, in 2001 and 2005, respectively. He is currently a Full Professor in applied mechanics with the Politecnico di Torino, Turin, Italy, after being a Professor in advanced vehicle engineering with the University of Surrey, Guildford, U.K., where he led the Centre for Automotive Engineering. His research interests include vehicle dynamics control for electric and automated vehicles.

Open Access funding provided by 'Politecnico di Torino' within the CRUI CARE Agreement